Journal of Computational Physics 372 (2018) 446–472

Contents lists available at ScienceDirect

Journal of Computational Physics

www.elsevier.com/locate/jcp

A compact fourth-order gas-kinetic scheme for the Euler and Navier–Stokes equations

Xing Ji [a], Liang Pan [c], Wei Shyy [b], Kun Xu [a,b,d,*]

[a] Department of Mathematics, Hong Kong University of Science and Technology, Clear Water Bay, Kowloon, Hong Kong
[b] Department of Mechanical and Aerospace Engineering, Hong Kong University of Science and Technology, Clear Water Bay, Kowloon, Hong Kong
[c] Institute of Applied Physics and Computational Mathematics, Beijing, 100088, China
[d] Shenzhen Research Institute, Hong Kong University of Science and Technology, Shenzhen 518057, China

ARTICLE INFO

Article history:
Received 10 December 2017
Received in revised form 3 June 2018
Accepted 11 June 2018
Available online 18 June 2018

Keywords:
Two-stage fourth-order discretization
Compact gas-kinetic scheme
High-order evolution model
Hermite WENO reconstruction

ABSTRACT

In this paper, a fourth-order compact gas-kinetic scheme (GKS) is developed for the compressible Euler and Navier–Stokes equations under the framework of two-stage fourth-order temporal discretization and Hermite WENO (HWENO) reconstruction. Due to the high-order gas evolution model, the GKS provides a time dependent gas distribution function at a cell interface. This time evolution solution can be used not only for the flux evaluation across a cell interface and its time derivative, but also time accurate flow variables at a cell interface. As a result, besides updating the conservative flow variables inside each control volume, the cell averaged slopes inside each control volume through the differences of flow variables at the cell interfaces can be updated as well in GKS. So, with the updated flow variables and their slopes inside each cell, the HWENO techniques can be naturally implemented for the compact high-order reconstruction at the beginning of each time step. Therefore, a compact higher-order GKS, such as the two-stage fourth-order compact scheme can be constructed. This fourth-order compact GKS has the same stencil and as robust as the second-order scheme. In comparison with the fourth-order DG method, they have the same stencil. In order to get a fourth-order temporal accuracy, the GKS uses two stages and DG needs four stages in the time stepping methods. The CFL number used in GKS is on the order of 0.5 instead of 0.11 in the DG. This research concludes that beyond the first-order Riemann solver the use of high-order time evolution model at a cell interface is extremely helpful in the design of robust, accurate, and efficient higher-order compact schemes for the compressible flow simulations.

1. Introduction

In past decades, there have been tremendous efforts on the development of higher-order numerical methods for hyperbolic conservation laws, and great success has been achieved. There are many review papers and monographs about the current status of higher-order schemes, which include essentially non-oscillatory scheme (ENO) [18,19,46,47], weighted essentially non-oscillatory scheme (WENO) [31,21], Hermite weighted essentially non-oscillatory scheme (HWENO) [41–43], and discontinuous Galerkin (DG) [9,10], etc. For the WENO and DG methods, two common ingredients are the use of Rie-

* Corresponding author at: Department of Mathematics, Hong Kong University of Science and Technology, Clear Water Bay, Kowloon, Hong Kong.
E-mail addresses: xjiad@connect.ust.hk (X. Ji), panliangjlu@sina.com (L. Pan), weishyy@ust.hk (W. Shyy), makxu@ust.hk (K. Xu).

https://doi.org/10.1016/j.jcp.2018.06.034
0021-9991/

mann solver for the interface flux evaluation [49] and the Runge–Kutta time-stepping for the high-order temporal accuracy [16]. In terms of spatial accuracy, WENO-type reconstruction can easily achieve very high order, i.e., up to 7th order while keeping good robustness [1]. However the WENO approach is based on large stencil and many cells are involved in the reconstruction, which makes the scheme complicated in the application to complex geometry with unstructured mesh. For the DG method, the most attractive property is its compactness. Even with second order scheme stencil, higher-order spatial accuracy can be achieved through the time evolution or direct update of higher-order spatial derivatives of flow variables. In the flow simulations with strong shocks, the DG methods seem to lack robustness. Great effort has been paid to limit the updated slopes or to find out the trouble cells beforehand. Still, the development of WENO and DG methods is one of the main research directions for the higher-order schemes.

In the above approaches, the first-order Riemann flux plays a key role for the flow evolution. Recently, instead of Riemann solver, many schemes based on the time-dependent flux functions have been developed, such as the Lax–Wendroff method [34], the generalized Riemann problem (GRP) [2–4], and ADER framework [49,11,12]. An outstanding method is the two-stage fourth order scheme for the Euler equations [26], where both the flux and time derivative of flux function are used in the construction of higher-order scheme. A compact fourth order scheme can be also constructed under the GRP framework for the hyperbolic equations [14]. Certainly, the two-stage fourth-order discretization has been used under other framework as well [45,8].

In the past years, the gas-kinetic scheme (GKS) has been developed systematically [53,54,56]. The flux evaluation in GKS is based on a time evolution solution of kinetic model for a physical process from the initial non-equilibrium state towards to an equilibrium one. In GKS, the spatial and temporal evolution of a gas distribution function is fully coupled nonlinearly. The comparison between GRP and GKS has been presented in [28] and the main difference is that GKS intrinsically provides a NS flux instead of inviscid one in GRP. The third-order and fourth-order GKS has been developed without using Runge–Kutta time stepping technique, but their flux formulations become extremely complicated [32,44,30], especially for multidimensional flow. Under the framework of multiple stages and multiple derivatives (MSMD) technique for numerical solution of ordinary differential equations [17], a two-stage fourth-order GKS with second-order flux function was constructed for the Euler and Navier–Stokes equations [39,40]. In comparison with the formal one-stage time-stepping third-order gas-kinetic solver [29,32], the fourth-order scheme not only reduces the complexity of the flux function, but also improves the accuracy of the scheme, although the third-order and fourth-order schemes take similar computational cost. The robustness of the two-stage fourth-order GKS is as good as the second-order shock capturing scheme. By combining the second-order or third-order GKS fluxes with MSMD technique again, a family of higher-order gas-kinetic methods has been constructed [20]. The above higher-order GKS uses the higher-order WENO reconstruction for spatial accuracy. These schemes are not compact and have room for further improvement.

The time dependent gas-distribution function in GKS at a cell interface provides not only the flux and its time derivative, but also time accurate flow variables at a cell interface. The design of compact GKS based on the cell averaged and cell interface values has been conducted before [52,37,38]. In the previous approach, the cell interface values are strictly enforced in the reconstruction, which may not be an appropriate approach. In this paper, inspired by the Hermite WENO (HWENO) reconstruction and compact fourth order GRP scheme [14], based on the interface values we are going to get the slopes of flow variables inside each control volume first, then based on the cell averaged values and slopes the HWENO reconstruction is implemented for the compact high-order reconstruction. The higher-order compact GKS developed in this paper is basically a unified combination of three ingredients, which are the two-stage fourth-order framework for temporal discretization [39], the higher-order gas evolution model for interface values and flux evaluations, and the HWENO reconstruction. In comparison with the GRP based fourth-order compact scheme, the current GKS provides the time accurate cell interface values one order higher in time than that in the GRP formulation. This fact makes the GKS more flexible to be extended to unstructured mesh, especially for the Navier–Stokes solutions.

The similarity and difference between the current compact fourth-order GKS and the fourth-order DG method include the followings. Both schemes are time explicit, have the same order of accuracy, and use the identical compact stencil and the HWENO reconstruction. However, the DG method uses the Runge–Kutta technique with four stages within each time step to get a fourth-order temporal accuracy, and the time step used in DG is on the order of CFL number 0.11 from stability requirement. For the fourth-order compact GKS, two stages are used for the same temporal accuracy due to the use of both flux and its time derivative, and the time step used in almost all calculations are on the order of CFL number 0.5. The updated slope in GKS comes from the explicit evolution solution of flow variables at the cell interfaces. The slope inside each cell is obtained through the Gauss's theorem from the interface values. But, the slopes in DG method are updated directly through weak formulation. The dynamic difference in slope update causes the GKS and DG methods to deviate from one another in terms of robustness in the capturing of discontinuous solutions. For the fourth-order compact GKS, the HWENO is fully implemented without using any additional trouble cell or limiting technique [50]. At end, the fourth-order compact GKS solves the NS equations naturally, it has the same robustness as the second-order shock capturing scheme, and it is much more efficient and robust than the same order DG method.

This paper is organized as follows. The brief review of the gas-kinetic flux solver is presented in Section 2. In Section 3, the general formulation for the two-stage temporal discretization is introduced. In Section 4, the compact gas-kinetic scheme with Hermite WENO reconstruction is given. Section 5 includes inviscid and viscous test cases to validate the current algorithm. The last section is the conclusion.

2. Gas-kinetic evolution model

The two-dimensional gas-kinetic BGK equation [5] can be written as

$$f_t + \mathbf{u}\cdot\nabla f = \frac{g-f}{\tau}, \tag{1}$$

where f is the gas distribution function, g is the corresponding equilibrium state, and τ is the collision time. The equilibrium state is a Maxwellian distribution

$$g_0 = \rho(\frac{\lambda}{\pi})^{\frac{K+2}{2}} e^{\lambda((u-U)^2+(v-V)^2+\xi^2)},$$

where $\lambda = m/2kT$, and m, k, T represent the molecular mass, the Boltzmann constant, and temperature, K is the number of internal degrees of freedom, i.e. $K = (4-2\gamma)/(\gamma-1)$ for two-dimensional flows, and γ is the specific heat ratio. The collision term satisfies the following compatibility condition

$$\int \frac{g-f}{\tau}\psi \mathrm{d}\Xi = 0, \tag{2}$$

where $\psi = (1, u, v, \frac{1}{2}(u^2+v^2+\xi^2))^T$, $\mathrm{d}\Xi = \mathrm{d}u\mathrm{d}v\mathrm{d}\xi_1 ... \mathrm{d}\xi_K$, the internal variable $\xi^2 = \xi_1^2 + \xi_2^2 + ... + \xi_K^2$. The connections between macroscopic mass ρ, momentum $(\rho U, \rho V)$, and energy ρE with the distribution function f are

$$\begin{pmatrix} \rho \\ \rho U \\ \rho V \\ \rho E \end{pmatrix} = \int \psi f d\Xi. \tag{3}$$

Similar kinetic models for quantum gases with equilibrium Bose–Einstein or Fermi–Dirac distributions have been constructed and studied as well [58].

Based on the Chapman–Enskog expansion for BGK equation [53], the gas distribution function in the continuum regime can be expanded as

$$f = g - \tau D_{\mathbf{u}} g + \tau D_{\mathbf{u}}(\tau D_{\mathbf{u}})g - \tau D_{\mathbf{u}}[\tau D_{\mathbf{u}}(\tau D_{\mathbf{u}})g] + ...,$$

where $D_{\mathbf{u}} = \partial/\partial t + \mathbf{u}\cdot\nabla$. By truncating on different orders of τ, the corresponding macroscopic equations can be derived. For the Euler equations, the zeroth order truncation is taken, i.e. $f = g$. For the Navier–Stokes equations, the first order truncated distribution function is

$$f = g - \tau(ug_x + vg_y + g_t).$$

Based on the higher order truncations, the Burnett and super-Burnett equations can be also derived [7,35,55].

Taking moments of the BGK equation Eq. (1) and integrating with respect to space, the semi-discrete finite volume scheme can be written as

$$\frac{\mathrm{d}W_{ij}}{\mathrm{d}t} = -\frac{1}{\Delta x}(F_{i+1/2,j}(t) - F_{i-1/2,j}(t)) - \frac{1}{\Delta y}(G_{i,j+1/2}(t) - G_{i,j-1/2}(t)),$$

where W_{ij} is the cell averaged value of conservative variables, $F_{i\pm1/2,j}(t)$ and $G_{i,j\pm1/2}(t)$ are the time dependent numerical fluxes at cell interfaces in x and y directions. The Gaussian quadrature is used to achieve the accuracy in space, such that

$$F_{i+1/2,j}(t) = \frac{1}{\Delta y}\int_{y_{j-1/2}}^{y_{j+1/2}} F_{i+1/2}(y,t)\mathrm{d}y = \sum_{\ell=1}^{2}\omega_\ell F_{i+1/2,j_\ell}(t), \tag{4}$$

where $\omega_1 = \omega_2 = 1/2$ are weights for the Gaussian quadrature points $y_{j_\ell} = y_j + \frac{(-1)^\ell}{2\sqrt{3}}\Delta y$, $\ell = 1, 2$, for a fourth-order accuracy. $F_{i+1/2,j_\ell}(t)$ are numerical fluxes and can be obtained as follows

$$F_{i+1/2,j_\ell}(t) = \int \psi u f(x_{i+1/2}, y_{j_\ell}, t, u, v, \xi)\mathrm{d}\Xi, \tag{5}$$

where $f(x_{i+1/2}, y_{j_\ell}, t, u, v, \xi)$ is the gas distribution function at the cell interface. In order to construct the numerical fluxes, the integral solution of BGK equation Eq. (1) is used

$$f(x_{i+1/2}, y_{j_\ell}, t, u, v, \xi) = \frac{1}{\tau}\int_0^t g(x', y', t', u, v, \xi)e^{-(t-t')/\tau}dt' + e^{-t/\tau} f_0(-ut, -vt, u, v, \xi), \tag{6}$$

where $(x_{i+1/2}, y_{j_\ell}) = (0, 0)$ is the location for flux evaluation, and $x_{i+1/2} = x' + u(t - t')$ and $y_{j_\ell} = y' + v(t - t')$ are the trajectory of particles. f_0 is the initial gas distribution function, g is the corresponding equilibrium state. The integral solution basically states a physical process from the particle free transport in f_0 in the kinetic scale to the hydrodynamic flow evolution in the integral of g term. The flow behavior at cell interface depends on the ratio of time step to the local particle collision time $\Delta t/\tau$.

To construct time evolution solution of a gas distribution function at a cell interface, the following notations are introduced first

$$\begin{aligned}
&a_1 = (\partial g/\partial x)/g, a_2 = (\partial g/\partial y)/g, A = (\partial g/\partial t)/g, B = (\partial A/\partial t),\\
&d_{11} = (\partial a_1/\partial x), d_{12} = (\partial a_1/\partial y) = (\partial a_2/\partial x), d_{22} = (\partial a_2/\partial y),\\
&b_1 = (\partial a_1/\partial t) = (\partial A/\partial x), b_2 = (\partial a_2/\partial t) = (\partial A/\partial y),
\end{aligned}$$

where g is an equilibrium state, and the dependence on particle velocities for each variable above, denoted as ω, can be expanded as [54]

$$\omega = \omega_1 + \omega_2 u + \omega_3 v + \omega_4 \frac{1}{2}(u^2 + v^2 + \xi^2).$$

The initial gas distribution function in Eq. (6) can be constructed as

$$f_0 = f_0^l(x, y, u, v)\mathbb{H}(x) + f_0^r(x, y, u, v)(1 - \mathbb{H}(x)),$$

where $\mathbb{H}(x)$ is the Heaviside function, f_0^l and f_0^r are the gas distribution functions on both sides of a cell interface at $t = 0$, which have one to one correspondence with the initially reconstructed macroscopic flow variables. For the third-order scheme, the Taylor expansion for the gas distribution function in space around $(x, y) = (0, 0)$ is expressed as

$$f_0^k(x, y) = f_G^k(0, 0) + \frac{\partial f_G^k}{\partial x}x + \frac{\partial f_G^k}{\partial y}y + \frac{1}{2}\frac{\partial^2 f_G^k}{\partial x^2}x^2 + \frac{\partial^2 f_G^k}{\partial x \partial y}xy + \frac{1}{2}\frac{\partial^2 f_G^k}{\partial y^2}y^2, \tag{7}$$

where $k = l, r$. According to the Chapman–Enskog expansion, f_G^k can be written as

$$f_G^k = g_k - \tau(a_{1k}u + a_{2k}v + A_k)g_k, \tag{8}$$

where g_l, g_r are the equilibrium states corresponding to the reconstructed macroscopic variables W_l, W_r. Substituting Eq. (7) and Eq. (8) into Eq. (6), the initial part for the integral solution can be written as

$$\begin{aligned}
&e^{-t/\tau} f_0^k(-ut, -vt, u, v, \xi)\\
&= C_7 g_k[1 - \tau(a_{1k}u + a_{2k}v + A_k)]\\
&+ C_8 g_k[a_{1k}u - \tau((a_{1k}^2 + d_{11k})u^2 + (a_{1k}a_{2k} + d_{12k})uv + (A_k a_{1k} + b_{1k})u)]\\
&+ C_8 g_k[a_{2k}v - \tau((a_{1k}a_{2k} + d_{12k})uv + (a_{2k}^2 + d_{22k})v^2 + (A_k a_{2k} + b_{2k})v)]\\
&+ \frac{1}{2}C_9[g_k(a_{1k}^2 + d_{11k})u^2 + 2(a_{1k}a_{2k} + d_{12k})uv + (a_{2k}^2 + d_{22k})v^2],
\end{aligned} \tag{9}$$

where the coefficients $a_{1k}, \ldots, A_k$, $k = l, r$ are defined according to the expansion of g_k. After determining the kinetic part f_0, the equilibrium state g in the integral solution Eq. (6) can be expanded in space and time as follows

$$\begin{aligned}
g = g_0 &+ \frac{\partial g_0}{\partial x}x + \frac{\partial g_0}{\partial y}y + \frac{\partial g_0}{\partial t}t + \frac{1}{2}\frac{\partial^2 g_0}{\partial x^2}x^2 + \frac{\partial^2 g_0}{\partial x \partial y}xy + \frac{1}{2}\frac{\partial^2 g_0}{\partial y^2}y^2\\
&+ \frac{1}{2}\frac{\partial^2 g_0}{\partial t^2}t^2 + \frac{\partial^2 g_0}{\partial x \partial t}xt + \frac{\partial^2 g_0}{\partial y \partial t}yt,
\end{aligned} \tag{10}$$

where g_0 is the equilibrium state located at a cell interface, which can be determined through the compatibility condition Eq. (2)

$$\int \psi g_0 \mathrm{d}\Xi = W^e = \int_{u>0} \psi g_l \mathrm{d}\Xi + \int_{u<0} \psi g_r \mathrm{d}\Xi, \tag{11}$$

where W^e are the macroscopic variables corresponding the equilibrium state g_0. Substituting Eq. (10) into Eq. (6), the hydrodynamic part for the integral solution can be written as

$$\begin{aligned}\frac{1}{\tau}\int_0^t g(x',y',t',u,v,\xi)e^{-(t-t')/\tau}dt' = {} & C_1 g_0 + C_2 g_0 \overline{a}_1 u + C_2 g_0 \overline{a}_2 v + C_3 g_0 \overline{A} + \frac{1}{2}C_5 g_0(\overline{A}^2 + \overline{B}) \\ & + \frac{1}{2}C_4[g_0(\overline{a}_1^2 + \overline{d}_{11})u^2 + 2(\overline{a}_1\overline{a}_2 + \overline{d}_{12})uv + (\overline{a}_2^2 + \overline{d}_{22})v^2] \\ & + C_6 g_0[(\overline{A}\overline{a}_1 + \overline{b}_1)u + (\overline{A}\overline{a}_2 + \overline{b}_2)v],\end{aligned} \tag{12}$$

where the coefficients $\overline{a}_1, \overline{a}_2, ..., \overline{A}, \overline{B}$ are defined from the expansion of equilibrium state g_0. The coefficients C_i, $i = 1, ..., 9$ in Eq. (9) and Eq. (12) are given by

$$\begin{aligned}& C_1 = 1 - e^{-t/\tau}, C_2 = (t+\tau)e^{-t/\tau} - \tau, C_3 = t - \tau + \tau e^{-t/\tau}, C_4 = -(t^2 + 2t\tau)e^{-t/\tau}, \\ & C_5 = t^2 - 2t\tau, C_6 = -t\tau(1 + e^{-t/\tau}), C_7 = e^{-t/\tau}, C_8 = -te^{-t/\tau}, C_9 = t^2 e^{-t/\tau}.\end{aligned}$$

The coefficients in Eq. (9) and Eq. (12) can be determined by the spatial derivatives of macroscopic flow variables and the compatibility condition as follows

$$\begin{cases}\langle a_1\rangle = \dfrac{\partial W}{\partial x}, \langle a_2\rangle = \dfrac{\partial W}{\partial y}, \langle A + a_1 u + a_2 v\rangle = 0, \\ \langle a_1^2 + d_{11}\rangle = \dfrac{\partial^2 W}{\partial x^2}, \langle a_2^2 + d_{22}\rangle = \dfrac{\partial^2 W}{\partial y^2}, \langle a_1 a_2 + d_{12}\rangle = \dfrac{\partial^2 W}{\partial x \partial y}, \\ \langle (a_1^2 + d_{11})u + (a_1 a_2 + d_{12})v + (Aa_1 + b_1)\rangle = 0, \\ \langle (a_2 a_1 + d_{21})u + (a_2^2 + d_{22})v + (Aa_2 + b_2)\rangle = 0, \\ \langle (Aa_1 + b_1)u + (Aa_2 + b_2)v + (A^2 + B)\rangle = 0,\end{cases} \tag{13}$$

where the superscripts or subscripts of these coefficients $a_1, ..., A, B$ are omitted for simplicity. More details about the determination of coefficient can be found in [29,32].

To improve the efficiency, a simplified third-order gas distribution function is used in this paper [60], which can be written as

$$\begin{aligned}f(x_{i+1/2}, y_{j_\ell}, t, u, v, \xi) = {} & g_0 + \bar{A}g_0 t + \frac{1}{2}\overline{a}_{tt} g_0 t^2 \\ & - \tau[(\overline{a}_1 u + \overline{a}_2 v + \overline{A})g_0 + (\overline{a}_{xt} u + \overline{a}_{yt} v + \overline{a}_{tt})g_0 t] \\ & - e^{-t/\tau} g_0[1 - (\overline{a}_1 u + \overline{a}_2 v)t] \\ & + e^{-t/\tau} g_l[1 - (a_{1l}u + a_{2l}v))t]H(u) \\ & + e^{-t/\tau} g_r[1 - (a_{1r}u + a_{2r}v))t](1 - H(u)),\end{aligned} \tag{14}$$

where the second-order derivatives are introduced as follows

$$\begin{aligned}& a_{xx} = g_{xx}/g, a_{xy} = g_{xy}/g, a_{yy} = g_{yy}/g, \\ & a_{xt} = g_{xt}/g, a_{yt} = g_{yt}/g, a_{tt} = g_{tt}/g.\end{aligned}$$

The determination of these coefficients is simplified as

$$\begin{cases}\langle a_{xx}\rangle = \dfrac{\partial^2 W}{\partial x^2}, \langle a_{xy}\rangle = \dfrac{\partial^2 W}{\partial x \partial y}, \langle a_{yy}\rangle = \dfrac{\partial^2 W}{\partial y^2}, \\ \langle a_{xx}u + a_{xy}v + a_{xt}\rangle = 0, \\ \langle a_{xy}u + a_{yy}v + a_{yt}\rangle = 0, \\ \langle a_{xt}u + a_{yt}v + a_{tt}\rangle = 0,\end{cases} \tag{15}$$

where the overline on these coefficients $a_{xx}, ..., a_{tt}$ are omitted as well. With the same third-order accuracy, the above simplified distribution function can speed up the flux calculation 4 times in comparison to the complete gas distribution function in 2-D case. Some basic formulas are given in Appendix C for the numerical implementation of the above flux solver.

For the non-compact two stages fourth-order scheme [39], theoretically a second-order gas-kinetic solver is enough for accuracy requirement, where the above third-order evolution solution reduces to the second-order one [54],

$$
\begin{aligned}
f(x_{i+1/2}, y_{j_\ell}, t, u, v, \xi) = {} & (1-e^{-t/\tau})g_0 + ((t+\tau)e^{-t/\tau} - \tau)(\bar{a}_1 u + \bar{a}_2 v)g_0 \\
& + (t - \tau + \tau e^{-t/\tau})\bar{A} g_0 \\
& + e^{-t/\tau} g_r[1 - (\tau + t)(a_{1r}u + a_{2r}v) - \tau A_r)]H(u) \\
& + e^{-t/\tau} g_l[1 - (\tau + t)(a_{1l}u + a_{2l}v) - \tau A_l)](1 - H(u)).
\end{aligned}
$$

3. Two-stage fourth-order temporal discretization

Recently, the two-stage fourth-order temporal discretization was developed for the generalized Riemann problem solver (GRP) [26] and gas-kinetic scheme (GKS) [39]. For conservation laws, the semi-discrete finite volume scheme is written as

$$
\frac{\mathrm{d}W_{ij}}{\mathrm{d}t} = -\frac{1}{\Delta x}(F_{i+1/2,j}(t) - F_{i-1/2,j}(t)) - \frac{1}{\Delta y}(G_{i,j+1/2}(t) - G_{i,j-1/2}(t)) := \mathcal{L}(W_{ij}),
$$

where $\mathcal{L}_{ij}(W)$ is the numerical operator for spatial derivative of flux, F and G are obtained by the Gaussian quadrature in Eq. (4). Then the semi-discretized finite volume scheme becomes a particular case of the general ODE system. With the following proposition, the two-stage fourth-order scheme can be developed.

Proposition 1. *Consider the following time-dependent equation*

$$
\frac{\partial W}{\partial t} = \mathcal{L}(W),
$$

with the initial condition at t_n, i.e.,

$$
W(t = t_n) = W^n,
$$

where $\mathcal{L}$ is an operator for spatial derivative of flux. A fourth-order temporal accurate solution for $W(t)$ at $t = t_n + \Delta t$ can be provided by

$$
W^* = W^n + \frac{1}{2}\Delta t \mathcal{L}(W^n) + \frac{1}{8}\Delta t^2 \frac{\partial}{\partial t}\mathcal{L}(W^n), \tag{16}
$$

$$
W^{n+1} = W^n + \Delta t \mathcal{L}(W^n) + \frac{1}{6}\Delta t^2\Big(\frac{\partial}{\partial t}\mathcal{L}(W^n) + 2\frac{\partial}{\partial t}\mathcal{L}(W^*)\Big), \tag{17}
$$

where the time derivatives are obtained by the Cauchy–Kovalevskaya method

$$
\begin{aligned}
&\frac{\partial W^n}{\partial t} = \mathcal{L}(W^n),\ \frac{\partial}{\partial t}\mathcal{L}(W^n) = \frac{\partial}{\partial W}\mathcal{L}(W^n)\mathcal{L}(W^n), \\
&\frac{\partial W^*}{\partial t} = \mathcal{L}(W^*),\ \frac{\partial}{\partial t}\mathcal{L}(W^*) = \frac{\partial}{\partial W}\mathcal{L}(W^*)\mathcal{L}(W^*).
\end{aligned}
$$

The details of proof can be found in [26].

For the gas-kinetic scheme, the gas evolution is a time-dependent relaxation process from kinetic to hydrodynamic scale through the exponential function, and the corresponding flux is a complicated function of time. In order to obtain the time derivatives of the flux function at t_n and $t_* = t_n + \Delta t/2$, the flux function can be approximated as a linear function of time within a time interval. Let's first introduce the following notation,

$$
\mathbb{F}_{i+1/2,j}(W^n, \delta) = \int_{t_n}^{t_n+\delta} \mathbf{F}_{i+1/2,j}(W^n, t)\mathrm{d}t.
$$

For convenience, assume $t_n = 0$, the flux in the time interval $[t_n, t_n + \Delta t]$ is expanded as the following linear form

$$
F_{i+1/2,j}(W^n, t) = F^n_{i+1/2,j} + t\partial_t F^n_{i+1/2,j}.
$$

The coefficients $F^n_{i+1/2,j}$ and $\partial_t F^n_{i+1/2,j}$ can be fully determined as follows

$$
\begin{aligned}
&F_{i+1/2,j}(W^n, t_n)\Delta t + \frac{1}{2}\partial_t F_{i+1/2,j}(W^n, t_n)\Delta t^2 = \mathbb{F}_{i+1/2,j}(W^n, \Delta t), \\
&\frac{1}{2}F_{i+1/2,j}(W^n, t_n)\Delta t + \frac{1}{8}\partial_t F_{i+1/2,j}(W^n, t_n)\Delta t^2 = \mathbb{F}_{i+1/2,j}(W^n, \Delta t/2).
\end{aligned}
$$

By solving the linear system, we have

$$\begin{aligned} F_{i+1/2,j}(W^n,t_n) &= (4\mathbb{F}_{i+1/2,j}(W^n,\Delta t/2)-\mathbb{F}_{i+1/2,j}(W^n,\Delta t))/\Delta t,\\ \partial_t F_{i+1/2,j}(W^n,t_n) &= 4(\mathbb{F}_{i+1/2,j}(W^n,\Delta t)-2\mathbb{F}_{i+1/2,j}(W^n,\Delta t/2))/\Delta t^2. \end{aligned} \tag{18}$$

Similarly, the numerical fluxes $G^n_{i,j+1/2}$ in the y-direction can be obtained as well. With the numerical fluxes and temporal derivatives, $\mathcal{L}(W^n_{ij})$ and $\frac{\partial}{\partial t}\mathcal{L}(W^n_{ij})$ can be given as follows

$$\begin{aligned} \mathcal{L}(W^n_{ij}) = &-\frac{1}{\Delta x}(F_{i+1/2,j}(W^n,t_n)-F_{i-1/2,j}(W^n,t_n))\\ &-\frac{1}{\Delta y}(G_{i,j+1/2}(Q^n,t_n)-G_{i,j-1/2}(Q^n,t_n)), \end{aligned} \tag{19}$$

$$\begin{aligned} \frac{\partial}{\partial t}\mathcal{L}(W^n_{ij}) = &-\frac{1}{\Delta x}(\partial_t F_{i+1/2,j}(W^n,t_n)-\partial_t F_{i-1/2,j}(W^n,t_n))\\ &-\frac{1}{\Delta y}(\partial_t G_{i,j+1/2}(W^n,t_n)-\partial_t G_{i,j-1/2}(W^n,t_n)). \end{aligned} \tag{20}$$

According to Eq. (16), W^*_{ij} at t_* can be updated. With the similar procedure, the numerical fluxes and temporal derivatives at the intermediate stage can be constructed and $\frac{\partial}{\partial t}\mathcal{L}(W^*_{ij})$ is given by

$$\begin{aligned} \frac{\partial}{\partial t}\mathcal{L}(W^*_{ij}) = &-\frac{1}{\Delta x}(\partial_t F_{i+1/2,j}(W^*,t_*)-\partial_t F_{i-1/2,j}(W^*,t_*))\\ &-\frac{1}{\Delta y}(\partial_t G_{i,j+1/2}(W^*,t_*)-\partial_t G_{i,j-1/2}(W^*,t_*)). \end{aligned} \tag{21}$$

According to Eq. (19), Eq. (20) and Eq. (21), W^{n+1}_{ij} at t_{n+1} can be updated by Eq. (17). Different from the Riemann problem with a constant state at a cell interface, the gas-kinetic scheme provides a time evolution solution. According to the relation in Eq. (3), the pointwise values at a cell interface can be obtained by taking moments of the time-dependent distribution function in Eq. (14)

$$W_{i+1/2,j_\ell}(t) = \int \psi f(x_{i+1/2}, y_{j_\ell}, t, u, v, \xi)\mathrm{d}\Xi. \tag{22}$$

Similar to the proposition for the two-stage temporal discretization, we have the following proposition for the time dependent gas distribution function at a cell interface

Proposition 2. *With the introduction of an intermediate state at $t_* = t_n + K\Delta t$,*

$$f^* = f^n + K\Delta t f^n_t + \frac{1}{2}K^2\Delta t^2 f^n_{tt}, \tag{23}$$

the state f^{n+1} is updated with the following formula

$$f^{n+1} = f^n + \Delta t(M_0 f^n_t + M_1 f^*_t) + \frac{1}{2}\Delta t^2\left(N_0 f^n_{tt} + N_1 f^*_{tt}\right), \tag{24}$$

and the solution f^{n+1} at $(t = t_n + \Delta t)$ has fourth-order accuracy with the following coefficients

$$K = \frac{1}{2}, M_0 = 1, M_1 = 0, N_0 = \frac{1}{3}, N_1 = \frac{2}{3}. \tag{25}$$

The proposition can be proved using the expansion

$$f^{n+1} = f^n + \Delta t f^n_t + \frac{\Delta t^2}{2}f^n_{tt} + \frac{\Delta t^3}{6}f^n_{ttt} + \frac{\Delta t^4}{24}f^n_{tttt} + \mathcal{O}(\Delta t^5).$$

According to the definition of the intermediate state, the above expansion becomes

$$\begin{aligned} f^{n+1} - f^n = &\Delta t(M_0+M_1)f^n_t + \frac{\Delta t^2}{2}(N_0+N_1+2M_1K)f^n_{tt}\\ &+\frac{\Delta t^3}{2}(M_1K^2+N_1K)f^n_{ttt} + \frac{\Delta t^4}{4}N_1K^2 f^n_{tttt} + \mathcal{O}(\Delta t^5). \end{aligned}$$

To have a fourth-order accuracy for the interface value at t^{n+1}, the coefficients are uniquely determined by Eq. (25). Therefore, the macroscopic variables $W^{n+1}_{i+1/2}$ at a cell interface can be obtained by taking moments of f^{n+1} and the cell interface values can be used for the reconstruction at the beginning of next time step.

In order to utilize the two-stage fourth-order temporal discretization for the gas distribution function, the third-order gas-kinetic solver is needed. To construct the first and second order time derivatives of the gas distribution function, the distribution function in Eq. (14) is approximated by the quadratic function

$$f(t) = f(x_{i+1/2}, y_{j_\ell}, t, u, v, \xi) = f^n + f_t^n(t - t^n) + \frac{1}{2} f_{tt}^n (t - t^n)^2.$$

According to the gas-distribution function at $t = 0$, $\Delta t/2$, and Δt

$$\begin{aligned}
&f^n = f(0),\\
&f^n + \frac{1}{2} f_t^n \Delta t + \frac{1}{8} f_{tt}^n \Delta t^2 = f(\Delta t/2),\\
&f^n + f_t^n \Delta t + f_{tt}^n \Delta t^2 = f(\Delta t),
\end{aligned}$$

the coefficients f^n, f_t^n and f_{tt}^n can be determined

$$\begin{aligned}
&f^n = f(0),\\
&f_t^n = (4f(\Delta t/2) - 3f(0) - f(\Delta t))/\Delta t,\\
&f_{tt}^n = 4(f(\Delta t) + f(0) - 2f(\Delta t/2))/\Delta t^2.
\end{aligned}$$

Thus, f^* and f^{n+1} are fully determined at the cell interface for the evaluation of macroscopic flow variables.

Remark 1. For smooth flow, the third-order time evolution solution in Eq. (14) reduces to

$$f(x_{i+1/2}, y_{j_\ell}, t, u, v, \xi) = g_0 + \overline{A} g_0 t + \frac{1}{2} \overline{a}_{tt} g_0 t^2.$$

The coefficients in Eq. (23) and Eq. (24) can be simplified as

$$\begin{aligned}
&f^n = g_0^n,\ f_t^n = \overline{A} g_0^n,\ f_{tt}^n = \overline{a}_{tt}^n g_0^n,\\
&f^* = g_0^*,\ f_t^* = \overline{A} g_0^*,\ f_{tt}^* = \overline{a}_{tt}^* g_0^*,
\end{aligned}$$

and the cell interface values $W_{i+1/2}^{n+1}$ become

$$W_{i+1/2}^{n+1} = \int \psi f^{n+1} d\Xi,$$

where the gas distribution function f^{n+1} has the form

$$f^{n+1} = g_0^n + \Delta t \overline{A} g_0^n + \frac{1}{6} \Delta t^2 (\overline{a}_{tt}^n g_0^n + 2\overline{a}_{tt}^* g_0^*).$$

Remark 2. For the scheme based on GRP in [14], the temporal evolution for the interface value is equivalent to

$$\begin{aligned}
&f^* = f^n + \frac{1}{2} \Delta t f_t^n,\\
&f^{n+1} = f^n + \Delta t f_t^*,
\end{aligned}$$

where a second-order evolution model is used at the cell interface. This is the two step Runge–Kutta method with second order time accuracy for the updated cell interface values at time step t^{n+1}. The order for the interface values in GRP is lower than that in GKS method. The method in [14] may have difficulty to get a compact 4th-order scheme on irregular mesh, such as unstructured one.

4. Implementation of HWENO reconstruction in GKS

The Hermite WENO (HWENO) is a reconstruction scheme based on the cell averaged flow variables and their slopes. The original HWENO reconstruction was developed as a compact limiter in DG scheme [41–43] for the hyperbolic conservation laws

$$W_t + F(W)_x = 0. \tag{26}$$

In original HWENO method, the evolution equation of slopes is obtained by taking additional spatial derivative on Eq. (26), which is

$$(W_x)_t + G(W, \Delta W)_x = 0, \tag{27}$$

where $G(W, \Delta W) = F'(W)W_x = F'(W)(W_x)$. After obtaining the updated flow variables and their slopes inside each cell, the HWENO reconstruction is directly applied to them to get the compact data reconstruction at the beginning of next time level. Even with the same HWENO reconstruction, the main difference between the above HWENO and GKS is about how to update the slopes inside each cell. Eq. (27) is directly used to update the slopes in HWENO.

In GKS, the spatial derivatives of flow variables inside each cell are calculated through the cell interface values with the help of Newton–Leibniz formula,

$$(W_x)_i = \frac{1}{\Delta x}\int_{I_i} \frac{\partial W}{\partial x}\mathrm{d}x = \frac{1}{\Delta x}(W_{i+1/2} - W_{i-1/2}), \tag{28}$$

where $W_{i+1/2}$ is provided by taking moments of the gas distribution function at the cell interface according to Eq. (24). Therefore, the GKS has both cell averaged values and slopes as well, but they are obtained in different way from the DG method. Then, the HWENO reconstruction, which is used in DG, can be directly applied to get initial data reconstruction in GKS. In the following, the HWENO reconstruction in GKS will be presented for initial data reconstruction from the updated flow variables and their slopes.

4.1. One-dimensional reconstruction

To reconstruct the left interface value $W^l_{i+1/2}$ at the cell interface $x_{i+1/2}$, three sub-stencils are selected

$$S_0 = \{I_{i-1}, I_i\}, \quad S_1 = \{I_i, I_{i+1}\}, \quad S_2 = \{I_{i-1}, I_i, I_{i+1}\}.$$

The Hermite quadratic reconstruction polynomials $w_k(x)$ corresponding to the substencil $S_k, k = 0, 1, 2$ are constructed according to the following conditions

$$\begin{aligned}
&\frac{1}{\Delta x}\int_{I_{i-j}} w_0(x)\mathrm{d}x = \overline{W}_{i-j}, \quad j = 0, 1, \quad \frac{1}{\Delta x}\int_{I_{i-1}} w_0'(x)\mathrm{d}x = (\overline{W}_x)_{i-1},\\
&\frac{1}{\Delta x}\int_{I_{i+j}} w_1(x)\mathrm{d}x = \overline{W}_{i+j}, \quad j = 0, 1, \quad \frac{1}{\Delta x}\int_{I_{i+1}} w_1'(x)\mathrm{d}x = (\overline{W}_x)_{i+1},\\
&\frac{1}{\Delta x}\int_{I_{i+j}} w_2(x)\mathrm{d}x = \overline{W}_{i+j}, \quad j = -1, 0, 1.
\end{aligned}$$

For the reconstructed polynomials, the point value at the cell interface $x_{i+1/2}$ can be given in terms of the cell averages value and the averaged spatial derivative as follows

$$\begin{aligned}
w_0(x_{i+1/2}) &= -\frac{7}{6}\overline{W}_{i-1} + \frac{13}{6}\overline{W}_i + \frac{2\Delta x}{3}(\overline{W}_x)_{i-1},\\
w_1(x_{i+1/2}) &= \frac{1}{6}\overline{W}_i + \frac{5}{6}\overline{W}_i + \frac{\Delta x}{3}(\overline{W}_x)_{i+1},\\
w_2(x_{i+1/2}) &= -\frac{1}{6}\overline{W}_{i-1} + \frac{5}{6}\overline{W}_i + \frac{1}{3}\overline{W}_{i+1}.
\end{aligned}$$

On the bigger stencil $\mathbb{T} = \{S_0, S_1, S_2\}$, a fourth-order reconstruction polynomial $W(x)$ are constructed according to the following conditions

$$\begin{aligned}
&\frac{1}{\Delta x}\int_{I_{i+j}} W(x)\mathrm{d}x = \overline{W}_{i+j}, \ j = -1, 0, 1,\\
&\frac{1}{\Delta x}\int_{I_{i+j}} W'(x)\mathrm{d}x = (\overline{W}_x)_{i+j}. \ j = -1, 1,
\end{aligned}$$

and the point value at the cell interface $x_{i+1/2}$ can be written as

$$W(x_{i+1/2}) = -\frac{23}{120}\overline{W}_{i-1} + \frac{19}{30}\overline{W}_i + \frac{67}{120}\overline{W}_{i+1} - \Delta x(\frac{3}{40}(\overline{W}_x)_{i-1} + \frac{7}{40}(\overline{W}_x)_{i+1}).$$

Similar to the classical WENO reconstruction, the linear weights γ_k, $k = 0, 1, 2$, can be found such that

$$W(x_{i+1/2}) = \sum_{k=0}^{2} \gamma_k w_k(x_{i+1/2}),$$

where $\gamma_0 = \frac{9}{80}, \gamma_1 = \frac{21}{40}, \gamma_2 = \frac{29}{80}$.

To deal with the discontinuity, the normalized nonlinear weight is introduced as follows

$$\omega_k = \frac{\overline{\omega}_k}{\sum_p \overline{\omega}_p}.$$

The non-normalized weights $\overline{\omega}_k$ is defined as follows

$$\overline{\omega}_k = \frac{\gamma_k}{(\beta_k + \epsilon)^2},$$

where β_k are the smoothness indicators. The reconstructed left interface value $W^l_{i+1/2}$ can be written as

$$W^l_{i+1/2} = \sum_{k=0}^{2} \overline{\omega}_k w_k(x_{i+1/2}).$$

More details of one-dimensional HWENO scheme can be found in [41].

With the same derivative reconstruction method in [32], a quadratic polynomial could be uniquely determined by $W^l_{i+1/2}$, $W^r_{i-1/2}$ and $\overline{W}_i$, where the derivatives of non-equilibrium part $(W_x)^l_{i+1/2}$, $(W_x)^r_{i-1/2}$, $(W_{xx})^l_{i+1/2}$, and $(W_{xx})^r_{i-1/2}$ can be obtained.

With the reconstructed $W^l_{i+1/2}$ and $W^r_{i+1/2}$ at both sides of a cell interface $x_{i+1/2}$, the macroscopic variables $W^e_{i+1/2}$ and the corresponding equilibrium state g_0 can be determined according to Eq. (11). To fully determine the slopes of the equilibrium state across the cell interface, the conservative variables across the cell interface is expanded as

$$w^e(x) = W^e_{i+1/2} + S_1(x - x_{i+1/2}) + \frac{1}{2}S_2(x - x_{i+1/2})^2 + \frac{1}{6}S_3(x - x_{i+1/2})^3 + \frac{1}{24}S_4(x - x_{i+1/2})^4.$$

With the following conditions,

$$\frac{1}{\Delta x}\int_{I_{i+k}} w^e(x)\mathrm{d}x = W_{i+k}, k = -1, ..., 2,$$

the derivatives are determined by

$$\begin{aligned}
(W_x)^e_{i+1/2} &= S_1 = \Big[-\frac{1}{12}(\overline{W}_{i+2} - \overline{W}_{i-1}) + \frac{5}{4}(\overline{W}_{i+1} - \overline{W}_i)\Big]/\Delta x, \\
(W_{xx})^e_{i+1/2} &= S_2 = \Big[-\frac{1}{8}(\overline{W}_{i+2} + \overline{W}_{i-1}) + \frac{31}{8}(\overline{W}_{i+1} + \overline{W}_i) - \frac{15}{2}W^e_{i+1/2}\Big]/\Delta x^2.
\end{aligned} \tag{29}$$

Thus, the reconstruction for the initial data and the equilibrium part are fully given in the one-dimensional case.

4.2. Two dimensional reconstruction

The direction by direction reconstruction strategy is applied on rectangular meshes [59]. The HWENO reconstruction can be extended to 2-D straightforward.

Before introducing the reconstruction procedure, let's denote $\overline{W}$ as cell averaged, $\hat{W}$ as line averaged, and W as pointwise values. Again $W^{l,r}$ represent the reconstructed quantities on the left and right sides of a cell interface, which correspond to the non-equilibrium initial part in GKS. Then, W^e is the reconstructed equilibrium state.

At t^n step, for cell (i, j) the cell average quantities $\overline{W}_{i,j}$, $(\overline{W}_x)_{i,j}$, $(\overline{W}_y)_{i,j}$ are stored. For a fourth order scheme, two Gaussian points on each interface are needed for numerical flux integration. Our target is to construct

$$\begin{aligned}
&W^l,\ W^l_x,\ W^l_y,\ W^l_{xx},\ W^l_{yy},\ W^l_{xy}, \\
&W^r,\ W^r_x,\ W^r_y,\ W^r_{xx},\ W^r_{yy},\ W^r_{xy}, \\
&W^e,\ W^e_x,\ W^e_y,\ W^e_{xx},\ W^e_{yy},\ W^e_{xy},
\end{aligned}$$

at each Gaussian point. To obtain these quantities, four line averaged sloped $(\hat{W}^n_x)_{i,j_l}$, $(\hat{W}^n_y)_{i_l,j}$ are additionally evaluated and stored, where $l = 1, 2$ represent the location Gaussian quadrature points in the corresponding direction. For a better illustration, a schematic is plotted in Fig. 1 and the reconstruction procedure for the Gaussian point $(i - 1/2, j_1)$ is summarized as follows. Here the time level n is omitted.

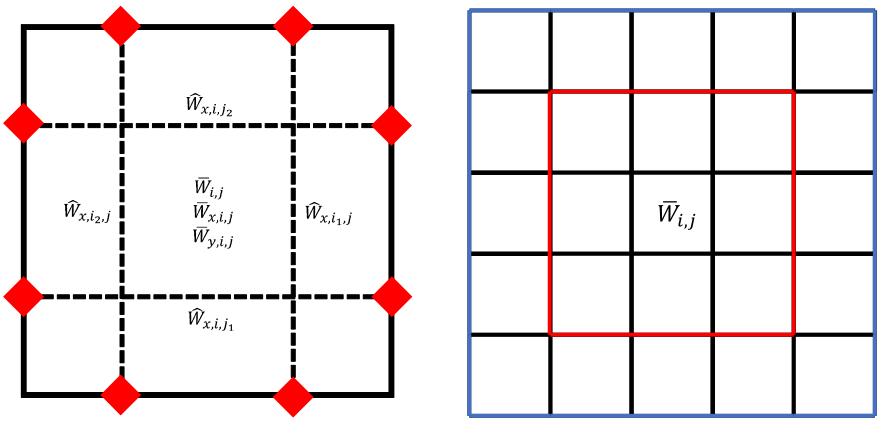

Fig. 1. The schematic for 2-D HWENO-GKS reconstruction. Left: Initial data for compact reconstruction at Gaussian points (in red color). Right: Reconstruction stencils for current compact HWENO GKS (red box with total 9 cells) and non-compact WENO GKS (blue box with total 25 cells). (For interpretation of the colors in the figure(s), the reader is referred to the web version of this article.)

Step 1. To obtain the line average values, i.e. $\hat{W}_{i,j_l}$, we perform HWENO reconstruction in tangential direction by using $\overline{W}_{i,j-1}, \overline{W}_{i,j}, \overline{W}_{i,j+1}$, and $(\overline{W}_y)_{i,j-1}, (\overline{W}_y)_{i,j+1}$. See Appendix A for details.

Step 2. With the reconstructed line average values i.e. $\hat{W}_{i-1,j_1}, \hat{W}_{i,j_1}, \hat{W}_{i+1,j_1}$ and original $(\hat{W}_x)_{i-1,j_1}, (\hat{W}_x)_{i+1,j_1}$, the one dimensional HWENO reconstruction is conducted and $W^r_{i-1/2,j_1}, W^l_{i+1/2,j_1}$ are obtained. With the same derivative reconstruction method in [32], $(W^r_x)_{i-1/2,j_1}, (W^l_x)_{i+1/2,j_1}$ and $(W^r_{xx})_{i-1/2,j_1}, (W^l_{xx})_{i+1/2,j_1}$ are constructed.

Step 3. The macro variables representing equilibrium state for each Gaussian point i.e. $W^e_{i-1/2,j_1}$ are obtained with $W^l_{i-1/2,j_1}, W^r_{i-1/2,j_1}$ by using Eq. (11). $(W^e_x)_{i-1/2,j_1}, (W^e_{xx})_{i-1/2,j_1}$ are calculated by Eq. (29).

Step 4. For the tangential derivatives, i.e. $(W^r_y)_{i-1/2,j_1}, (W^r_{yy})_{i-1/2,j_1}$, a WENO-type reconstruction is adopted by using $W^r_{i-1/2,(j-1)_2}, W^r_{i-1/2,j_1}, W^r_{i-1/2,j_2}, W^r_{i-1/2,(j+1)_1}$, see the Appendix B. And $(W^r_{xy})_{i-1/2,j_1}$ could be obtained in the same way with corresponding W^r_x.

Step 5. For the equilibrium state, a smooth third-order polynomial can be constructed by $W^e_{i-1/2,(j-1)_2}, W^e_{i-1/2,j_1}$, $W^e_{i-1/2,j_2}, W^e_{i-1/2,(j+1)_1}$, and the tangential derivatives, i.e. $(W^e_y)_{i-1/2,j_1}, (W^e_{yy})_{i-1/2,j_1}$ are obtained. Then, $(W^e_{xy})_{i-1/2,j_1}$ can be determined in the same way as for the corresponding W^e_x.

Similar procedure can be performed to obtain all needed values at each Gaussian point.

After gas evolution process, the updated cell interface values are obtained, i.e. $W^*_{i\pm1/2,j_l}$, $W^*_{i_l,j\pm1/2}$ at time $t = t^*$. Then the cell averaged values are computed through conservation laws by Eq. (16). And according to the Gauss's theorem the cell averaged slopes can be updated using

$$\overline{W}^*_{x,i,j} = \frac{1}{\Delta x}\sum_{l=1}^{2}(W^*_{i+1/2,j_l} - W^*_{i-1/2,j_l}),$$

$$\overline{W}^*_{y,i,j} = \frac{1}{\Delta y}\sum_{l=1}^{2}(W^*_{i_l,j+1/2} - W^*_{i_l,j-1/2}),$$

where W^* at cell interfaces are obtained by taking moments of the gas distribution function at that location and time.

Lastly, in the rectangular case, the line averaged slopes are approximated by

$$\hat{W}^*_{x,i,j_l} = \frac{1}{\Delta x}(W^*_{i+1/2,j_l} - W^*_{i-1/2,j_l}),$$
$$\hat{W}^*_{y,i_l,j} = \frac{1}{\Delta y}(W^*_{i_l,j+1/2} - W^*_{i_l,j-1/2}).$$

5. Numerical examples

In this section, numerical tests will be presented to validate the compact 4th-order GKS. For the inviscid flow, the collision time τ is

$$\tau = \epsilon\Delta t + C|\frac{p_l - p_r}{p_l + p_r}|\Delta t,$$

Table 1
Advection of density perturbation: accuracy test for the cell interface values in reconstructions.

Mesh	L^1 error	Convergence order	L^2 error	Convergence order
10	1.2797E−003		9.8877E−004	
20	7.2353E−005	4.1446	5.6650E−005	4.1254
40	3.3806E−006	4.4196	2.6547E−006	4.4154
80	1.2863E−007	4.7159	1.0100E−007	4.7160
160	4.3188E−009	4.8965	3.3919E−009	4.8962
320	1.3819E−010	4.9658	1.0854E−010	4.9657
640	4.3517E−012	4.9890	3.4184E−012	4.9887

where $\varepsilon = 0.01$ and $C = 1$. For the viscous flow, the collision time is related to the viscosity coefficient,

$$\tau = \frac{\mu}{p} + C|\frac{p_l - p_r}{p_l + p_r}|\Delta t,$$

where p_l and p_r denote the pressure on the left and right sides of the cell interface, μ is the dynamic viscous coefficient, and p is the pressure at the cell interface. In smooth flow regions, it will reduce to $\tau = \mu/p$. The ratio of specific heats takes $\gamma = 1.4$. The reason for including pressure jump term in the particle collision time is to add artificial dissipation in the discontinuous region to enlarge the shock thickness to the scale of numerical cell size, and to keep the non-equilibrium dynamics in the shock layer through the kinetic particle transport to mimic the real physical mechanism. For turbulent flow simulations, the above collision time has to be modified with the inclusion of turbulence viscosity coefficient μ_t [27], such as $\tau = (\mu + \mu_t)/p$.

Same as many other higher-order schemes, all reconstructions will be done on the characteristic variables. Denote $F(W) = (\rho U, \rho U^2 + p, \rho UV, U(\rho E + p))$ in the local coordinate. The Jacobian matrix $\partial F/\partial W$ can be diagonalized by the right eigenmatrix R. For a specific cell interface, R_* is the right eigenmatrix of $\partial F/\partial W^*$, and W^* are the averaged conservative flow variables from both sides of the cell interface. The characteristic variables for reconstruction are defined as $U = R_*^{-1}W$.

The current compact 4th-order GKS is compared with the non-compact 4th-order WENO-GKS in [39,36]. Both schemes take the same two Gaussian points at each cell interface in 2D case, and two stage fourth order time marching strategy for flux evaluation. The reconstruction is based on characteristic variables for both schemes and uses the same type non-linear weights of WENO-JS [21] in most cases. The main difference between them is on the initial data reconstruction, where the large stencils are used in the normal WENO-GKS and the local interface values are adopted in the compact HWENO-GKS.

5.1. Accuracy tests

The advection of density perturbation is tested, and the initial condition is given as follows

$$\rho(x) = 1 + 0.2\sin(\pi x), \quad U(x) = 1, \quad p(x) = 1, x \in [0, 2].$$

With the periodic boundary condition, the analytic solution is

$$\rho(x, t) = 1 + 0.2\sin(\pi(x - t)), \quad U(x, t) = 1, \quad p(x, t) = 1.$$

In the computation, a uniform mesh with N points is used. The time step $\Delta t = 0.2\Delta x$ is fixed. Before the full scheme using HWENO is tested, the order of accuracy for the cell interface values will be validated firstly. Here instead of using HWENO, we are going to use the cell interface values directly in the reconstruction for the compact GKS scheme. Based on the compact stencil,

$$S = \{\overline{W}_{i-1}, W_{i-1/2}, \overline{W}_i, W_{i+1/2}, \overline{W}_{i+1}\}$$

with three cell averaged values and two cell interface values, a fourth-order polynomial $W(x)$ can be constructed according to the following constraints

$$\int_{I_{i+l}} W(x)\mathrm{d}x = W_{i+l}, l = -1, 0, 1, \quad W(x_{i+m-1/2}) = W_{i+m-1/2}, m = 0, 1,$$

where the cell interface value $W(x_{i+1/2})$ is equal to $W_{i+1/2}$ exactly. Based on the above reconstruction, the compact scheme is expected to present a fifth-order spatial accuracy and a fourth-order temporal accuracy. The L^1 and L^2 errors and orders at $t = 2$ are given in Table 1. This test shows that the cell interface updated values have the expected accuracy, which can be used in the spatial reconstruction. Next, the full compact GKS is tested using the HWENO reconstruction, where the interface values are transferred into the cell averaged slopes. For the HWENO compact GKS, the L^1 and L^2 errors and order of accuracy at $t = 2$ are shown in Table 2. With the mesh refinement, the expected order of accuracy is obtained as well.

Table 2
Advection of density perturbation: accuracy test for HWENO compact GKS method at smooth reconstruction.

Mesh	L^1 error	Convergence order	L^2 error	Convergence order
10	2.666501E−04		2.094924E−04	
20	1.082129E−05	4.6228	8.693374E−06	4.5908
40	5.530320E−07	4.2904	4.967487E−07	4.1293
80	3.251087E−08	4.0884	2.940079E−08	4.0786
160	1.971503E−09	4.0436	1.769347E−09	4.0546
320	1.210960E−10	4.0250	1.081183E−10	4.0325
640	7.497834E−12	4.0135	6.675859E−12	4.0175

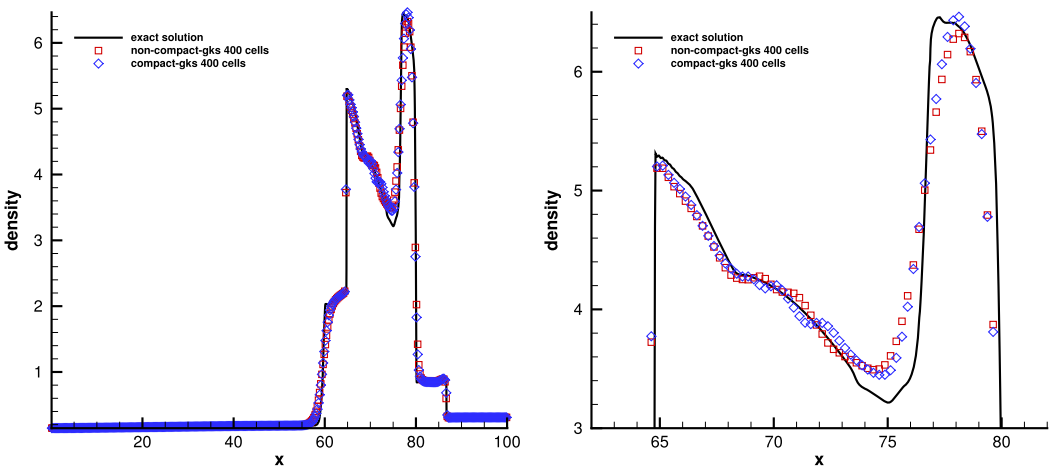

Fig. 2. Blast wave problem: the density distribution and local enlargement at $t = 3.8$ with 400 cells.

5.2. One dimensional Riemann problems

The first case is the Woodward–Colella blast wave problem [51], and the initial conditions are given as follows

$$(\rho, U, p) = \begin{cases} (1, 0, 1000), & 0 \le x < 10, \\ (1, 0, 0.01), & 10 \le x < 90, \\ (1, 0, 100), & 90 \le x \le 100. \end{cases}$$

The computational domain is $[0, 100]$, and the reflected boundary conditions are imposed on both ends. The computed density profile and local enlargement with 400 mesh points and the exact solution at $t = 3.8$ are shown in Fig. 2. The numerical results agree well with the exact solutions. The scheme can resolve the wave profiles well, particularly for the local extreme values.

The second one is the Shu–Osher problem [47], and the initial conditions are

$$(\rho, U, p) = \begin{cases} (3.857134, 2.629369, 10.33333), & -5 < x \le -4, \\ (1 + 0.2\sin(5x), 0, 1), & -4 < x < 5. \end{cases}$$

As an extension of the Shu–Osher problem, the Titarev–Toro problem [48] is tested as well, and the initial condition in this case is the following

$$(\rho, U, p) = \begin{cases} (1.515695, 0.523346, 1.805), & -5 < x \le -4.5, \\ (1 + 0.1\sin(20\pi x), 0, 1), & -4.5 < x < 5. \end{cases}$$

In these two cases, the computational domain is $[-5, 5]$. The non-reflecting boundary condition is imposed on left end, and the fixed wave profile is given on the right end. Both compact GKS with HWENO and non-compact GKS with fifth-order WENO are tested for these two cases. The computed density profiles, local enlargements, and the exact solutions for the Shu–Osher problem with 400 mesh points at $t = 1.8$ and the Titarev–Toro problem with 1000 mesh points at $t = 5$ are shown in Fig. 3 and Fig. 4, respectively. Titarev–Toro problem is sensitive to reconstruction scheme [6,14]. Instead of WENO-JS used above for non-linear weights, the WENO-Z weights can keep the same order of accuracy in extreme points. Combining the HWENO-Z reconstruction and the compact GKS, the result is shown in Fig. 5, which can be compared with the solution from the GRP method [14].

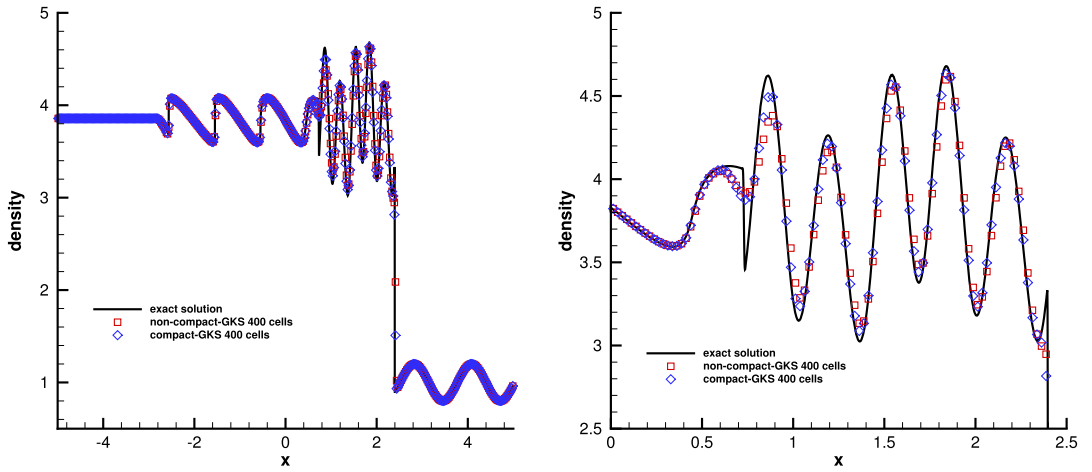

Fig. 3. Shu–Osher problem: the density distributions and local enlargement at $t = 1.8$ with 400 cells.

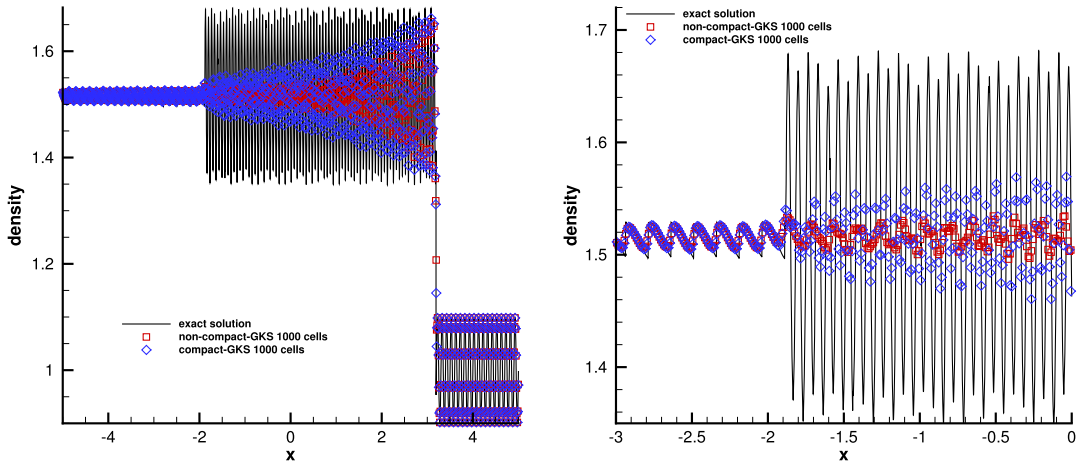

Fig. 4. Titarev–Toro problem: the density distributions and local enlargement at $t = 5$ with 1000 cells.

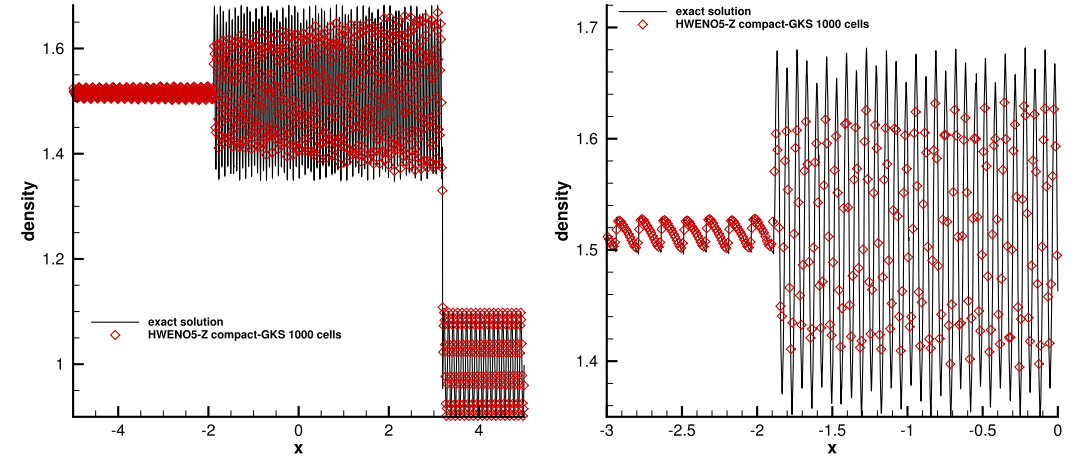

Fig. 5. Titarev–Toro problem: the results by using HWENO-Z reconstruction.

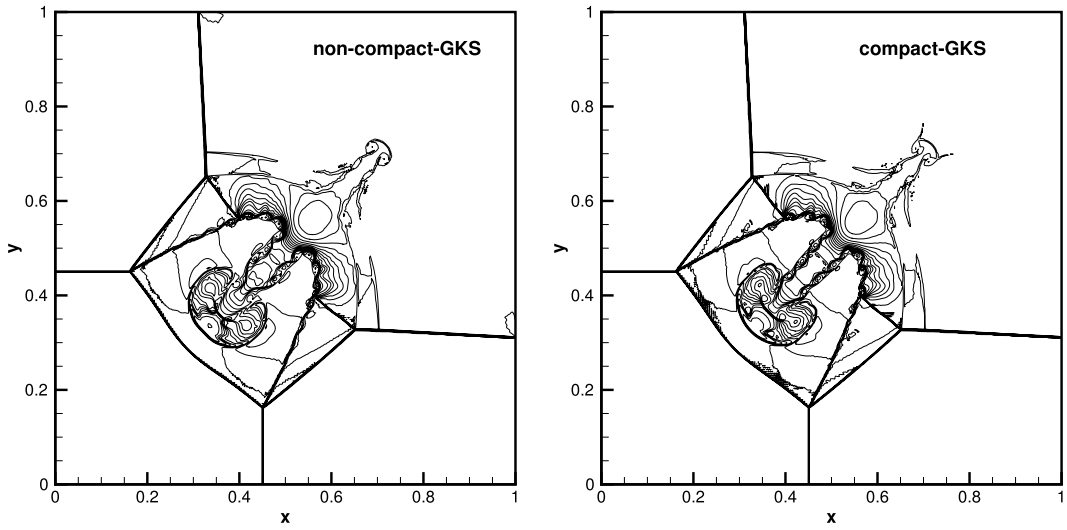

Fig. 6. Two-dimensional Riemann problem: the density distribution of four shock-interaction at $t = 0.6$.

5.3. Two-dimensional Riemann problems

In the following, two examples of two-dimensional Riemann problems are considered [33], which involve the interactions of shocks and the interaction of contact continuities. The computational domain $[0, 1] \times [0, 1]$ is covered by 500×500 uniform mesh points, where non-reflecting boundary conditions are used in all boundaries. The initial conditions for the first problem are

$$(\rho, U, V, p) = \begin{cases} (1.5, 0, 0, 1.5), & x > 0.7, y > 0.7, \\ (0.5323, 1.206, 0, 0.3), & x < 0.7, y > 0.7, \\ (0.138, 1.206, 1.206, 0.029), & x < 0.7, y < 0.7, \\ (0.5323, 0, 1.206, 0.3), & x > 0.7, y < 0.7. \end{cases}$$

Four initial shock waves interact with each other and result in a complicated flow pattern. The density distributions calculated by compact and non-compact GKS with HWENO and WENO reconstructions are presented at $t = 0.6$ in Fig. 6. From the analysis in [33], the initial shock wave S_{23}^{-} bifurcates at the trip point into a reflected shock wave, a Mach stem, and a slip line. The reflecting shock wave interacts with the shock wave S_{12}^{-} to produce a new shock. The small scale flow structures are well resolved by the current scheme.

The initial conditions for the second 2-D Riemann problem are

$$(\rho, U, V, p) = \begin{cases} (1, 0.1, 0.1, 1), & x > 0.5, y > 0.5, \\ (0.5197, -0.6259, 0.1, 0.4), & x < 0.5, y > 0.5, \\ (0.8, 0.1, 0.1, 0.4), & x < 0.5, y < 0.5, \\ (0.5197, 0.1, -0.6259, 0.4), & x > 0.5, y < 0.5. \end{cases}$$

This case is to simulate the shear instabilities among four initial contact discontinuities. The density distributions calculated by compact and non-compact GKS with HWENO and WENO reconstructions are presented at $t = 0.8$ in Fig. 7. The results indicate that the current HWENO compact GKS resolves the Kelvin–Helmholtz instabilities better.

5.4. Double Mach reflection problem

This problem was extensively studied by Woodward and Colella [51] for the inviscid flow. The computational domain is $[0, 4] \times [0, 1]$, and a solid wall lies at the bottom of the computational domain starting from $x = 1/6$. Initially a right-moving Mach 10 shock is positioned at $(x, y) = (1/6, 0)$, and makes a 60° angle with the x-axis. The initial pre-shock and post-shock conditions are

$$(\rho, U, V, p) = (8, 4.125\sqrt{3}, -4.125, 116.5),$$
$$(\rho, U, V, p) = (1.4, 0, 0, 1).$$

The reflecting boundary condition is used at the wall. While for the rest of bottom boundary, the exact post-shock condition is imposed. At the top boundary, the flow variables are set to follow the motion of the Mach 10 shock. The density distributions and local enlargement with 960×240 and 1920×480 uniform mesh points at $t = 0.2$ with HWENO reconstructions

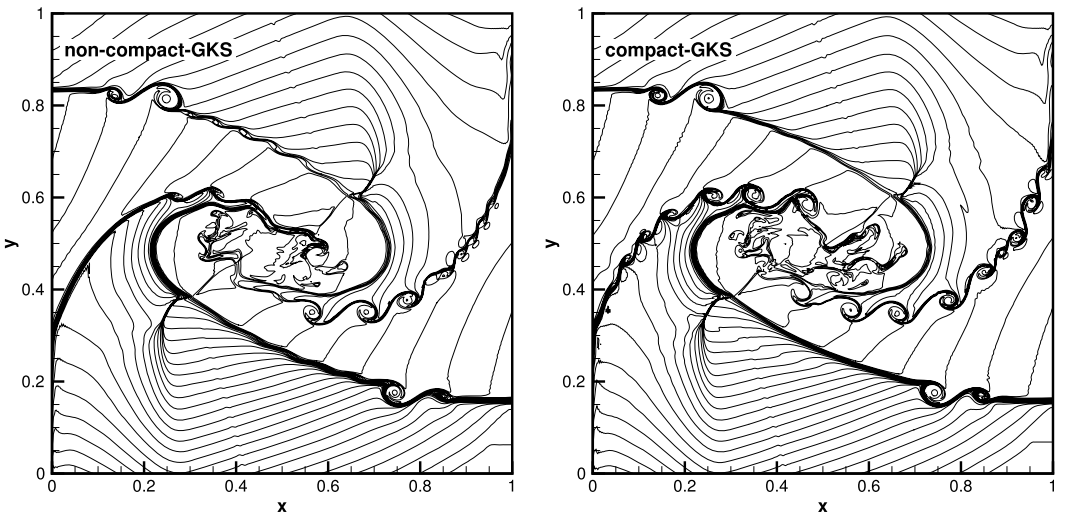

Fig. 7. Two-dimensional Riemann problem: the density distribution of four contact discontinuities-interaction at $t = 0.8$.

are shown in Fig. 8 and Fig. 9. The robustness of the compact GKS is validated, and the flow structure around the slip line from the triple Mach point is resolved better by the compact scheme.

5.5. Viscous shock tube problem

This problem was introduced to test the performances of different schemes for viscous flows [13]. In this case, an ideal gas is at rest in a two-dimensional unit box $[0, 1] \times [0, 1]$. A membrane located at $x = 0.5$ separates two different states of the gas and the dimensionless initial states are

$$(\rho, U, p) = \begin{cases} (120, 0, 120/\gamma), & 0 < x < 0.5, \\ (1.2, 0, 1.2/\gamma), & 0.5 < x < 1, \end{cases}$$

where $\gamma = 1.4$ and Prandtl number $Pr = 0.73$.

The membrane is removed at time zero and wave interaction occurs. A shock wave, followed by a contact discontinuity, moves to the right with Mach number $Ma = 2.37$ and reflects at the right end wall. After the reflection, it interacts with the contact discontinuity. The contact discontinuity and shock wave interact with the horizontal wall and create a thin boundary layer during their propagation. The solution will develop complex two-dimensional shock/shear/boundary-layer interactions. This case is tested in the computational domain $[0, 1] \times [0, 0.5]$, a symmetric boundary condition is used on the top boundary $x \in [0, 1]$, $y = 0.5$. Non-slip boundary condition, and adiabatic condition for temperature are imposed at solid wall. Firstly, the Reynolds number $Re = 200$ case is tested. For this case with $Re = 200$, the density distributions with 500×250 uniform mesh points at $t = 1.0$ from non-compact and compact GKS with HWENO and WENO reconstructions are shown in Fig. 10. The density profiles along the lower wall for this case are presented in Fig. 11. As a comparison, the results from WENO reconstruction with 1000×500 uniform mesh points is given as well, which agrees well with the density profiles provided by compact GKS with HWENO method and 500×250 mesh points. As shown in Table 3, the height of primary vortex predicted by the current compact scheme agrees well with the reference data [22].

Secondly, the $Re = 1000$ case is computed with different girds. As shown in Fig. 12, the vortex shedding could be observed clearly at the wedge-shaped area defined in [23] with 1000×500 and 2000×1000 mesh points. The density distribution along the wall at $t = 1.0$ is plotted in Fig. 13. In comparison with the reference result of two-stage fourth-order GKS [39], the density distribution along the wall agree well with traditional non-compact WENO GKS.

Based on the above tests, we can realize the robustness and accuracy of the compact 4th-order GKS. The scheme will be used in the real engineering applications, such as the turbulent transition [24,25].

5.6. Lid-driven cavity flow

In order to further test the scheme in the capturing of viscous flow solution, the lid-driven cavity problem is one of the most important benchmarks for validating incompressible Navier–Stokes flow solvers. The fluid is bounded by a unit square and is driven by a uniform translation of the top boundary. In this case, the flow is simulated with Mach number $Ma = 0.15$ and all boundaries are isothermal and nonslip. The computational domain $[0, 1] \times [0, 1]$ is covered with 65×65 mesh points. Numerical simulations are conducted for two different Reynolds numbers, i.e., $Re = 400$ and 1000. The streamlines are shown in Fig. 14. The U-velocities along the center vertical line, and V-velocities along the center horizontal line, are shown in Fig. 15. The benchmark data [15] for $Re = 400$ and 1000 are also presented, and the simulation results match

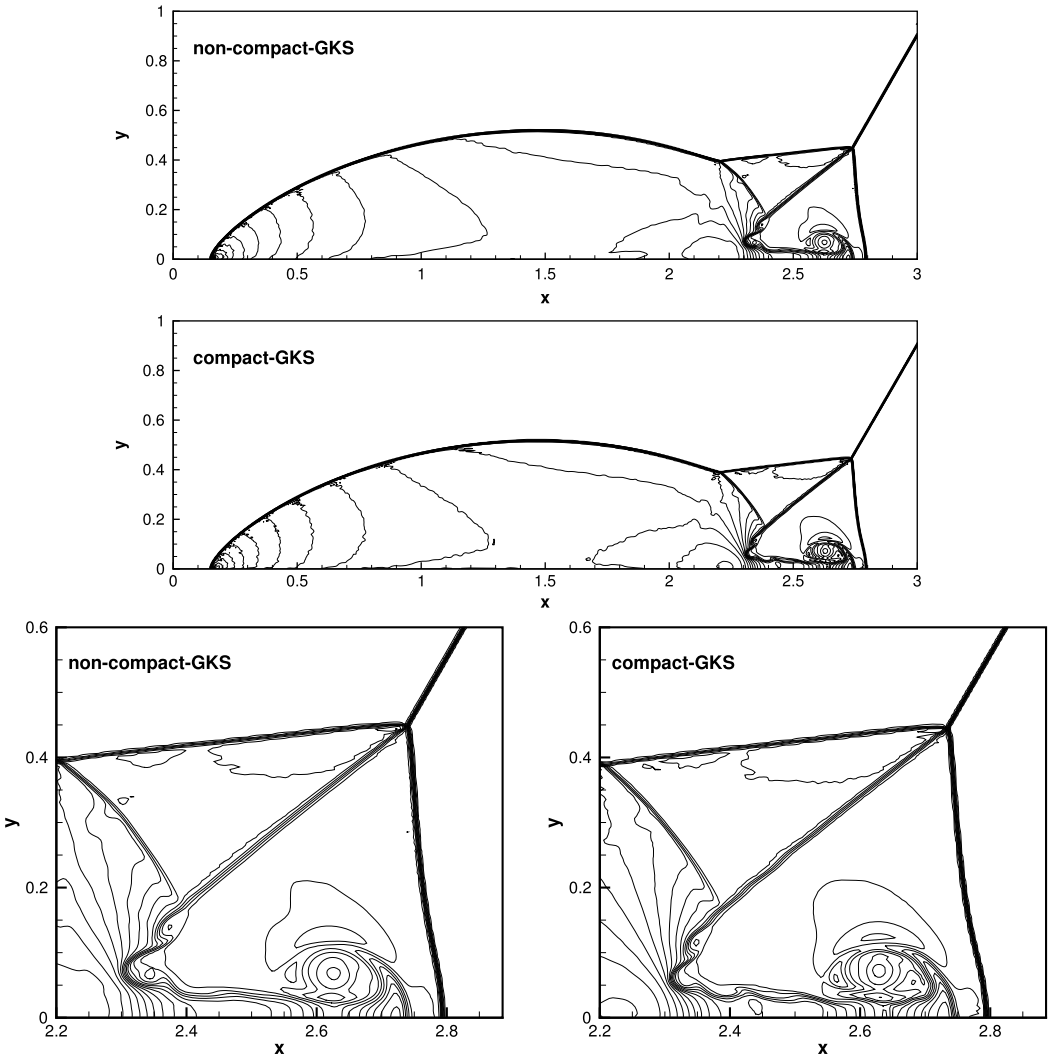

Fig. 8. Double Mach reflection: density contours from compact and non-compact GKS with HWENO and WENO reconstructions and 960×240 mesh points.

well with these benchmark data. The cavity case fully validates the higher-order accuracy of the compact GKS. With 65×65 mesh points, second-order schemes cannot get such accurate solutions.

6. Conclusion

In this paper, a fourth-order compact gas-kinetic scheme based on Hermite WENO reconstruction is presented. The construction of such a compact higher-order scheme is solely due to the use of the updated cell interface values, i.e., the so-called strong evolution solution, from which the cell averaged slopes inside each cell can be obtained. Then, based on the cell averaged flow variables and their slopes, the HWENO reconstruction can be naturally implemented here. There are similarity and differences between the current GKS and the 4th-order DG method. Both schemes have the same order accuracy and use the same HWENO reconstruction with the same compactness of the stencil. The main difference between these two methods is that for the DG method the slope at time step t^{n+1} is obtained through time evolution equation of the slope directly. However, for the GKS the cell interface flow variables are evolved first, then the slope inside each control volume at t^{n+1} is obtained by applying Gauss's law through the interface values. More specifically, in the DG method the cell averaged values and their slopes are evolved separately with distinguishable discretized governing equations, while in the GKS the updates of both cell averaged values and their slopes are coming from the same time-dependent gas distribution function for the fluxes and the interface values, which is coming from a time accurate evolution solution of the kinetic model. There is no direct evolution equation for slopes in GKS. The DG is based on the weak formulation with the involvement of test function, the GKS is based on the strong solution, which is unique from the kinetic model equation and the initial reconstruction. For the 4th-order accuracy, the DG uses the Runge–Kutta time stepping scheme with four stages within each time

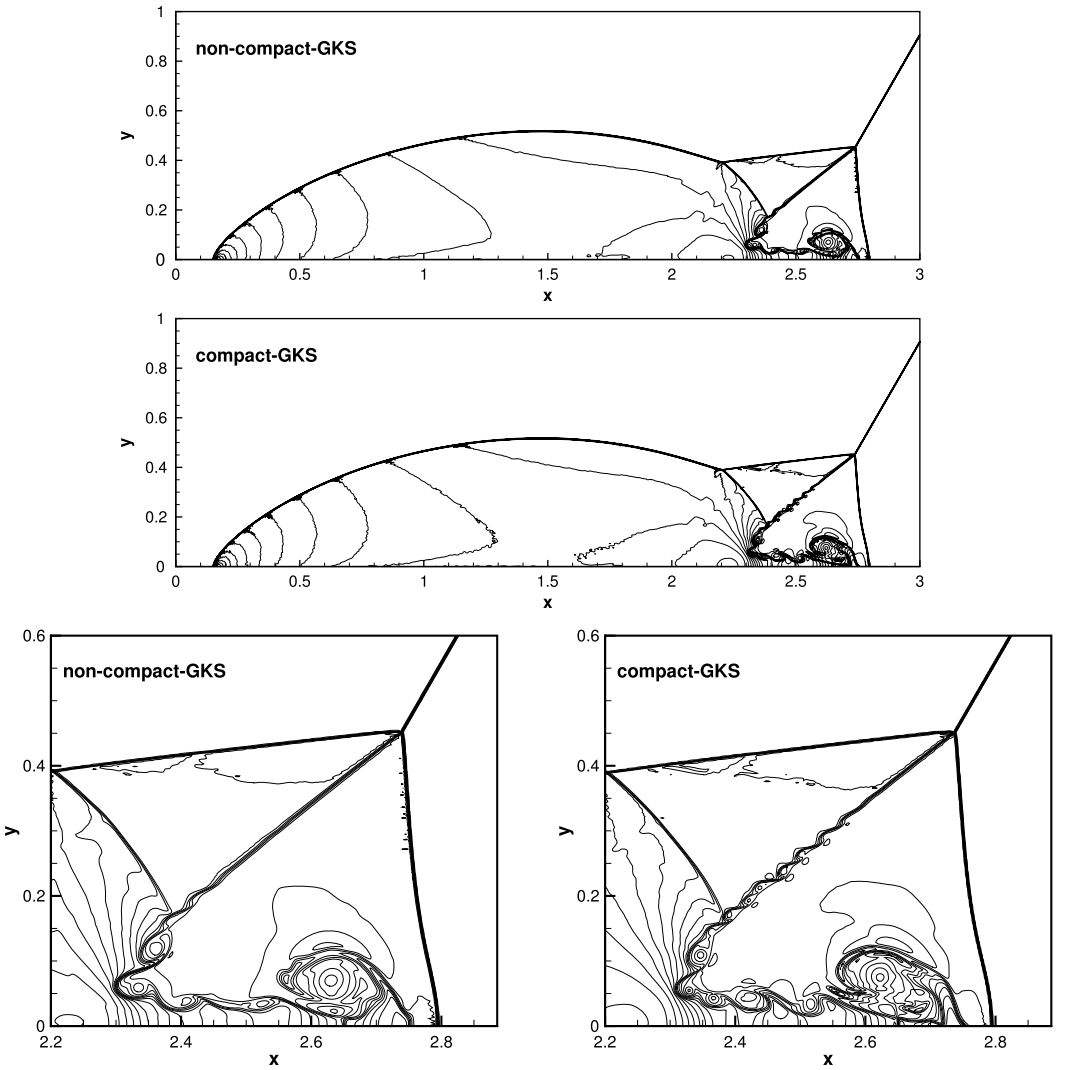

Fig. 9. Double Mach reflection: local enlargement of density contours from compact and non-compact GKS with HWENO and WENO reconstructions and 1920×480 mesh points.

step and has a CFL number limitation of 0.11 from the stability consideration. For the same order accuracy, the GKS only involves two stages and the CFL number for the time step can be on the order of 0.5. Even with the expensive GKS flux function targeting on the Navier–Stokes solutions, the computational efficiency of the GKS is much higher than that of the DG method for the Euler and Navier–Stokes equations. Based on the test cases in this paper and many others not presented here, the 4th-order compact GKS has the same robustness as the 2nd-order shock capturing schemes, where there are no trouble cells and any other special limiting process involved in the GKS calculations. The current paper only presents the compact scheme on structured rectangular mesh. Following the approach of the 3rd-order compact GKS on unstructured mesh [37], the 4th-order compact GKS with two stages within a time step will be constructed on unstructured mesh as well.

The present research clearly indicates that the dynamics of the 1st-order Riemann solver is not enough for the construction of truly higher-order schemes. Theoretically, from physical point of view, the development of compact scheme is the direction for CFD algorithm, because from the kinetic particle transport to the hydrodynamic wave propagation there is limited physical propagating speed [57], and the fluid element only has dynamic connection with neighbors. The CFL number is not only for the determination of time step, but also quantifies the relative physical domain of dependence with respect to the numerical one. Ideally, the numerical domain of dependence for any scheme, i.e., lower or higher orders, should be the same as the physical domain of dependence, rather than the large disparity between them in the current existing schemes, such as the very large numerical domain of dependence (large stencils) in the WENO approach and the severely confined CFL number in the DG method. This discrepancy is coming from the inconsistency between the first-order Riemann solver and the higher-order dynamics requirement in the higher-order schemes. The large difference in the domain of dependence

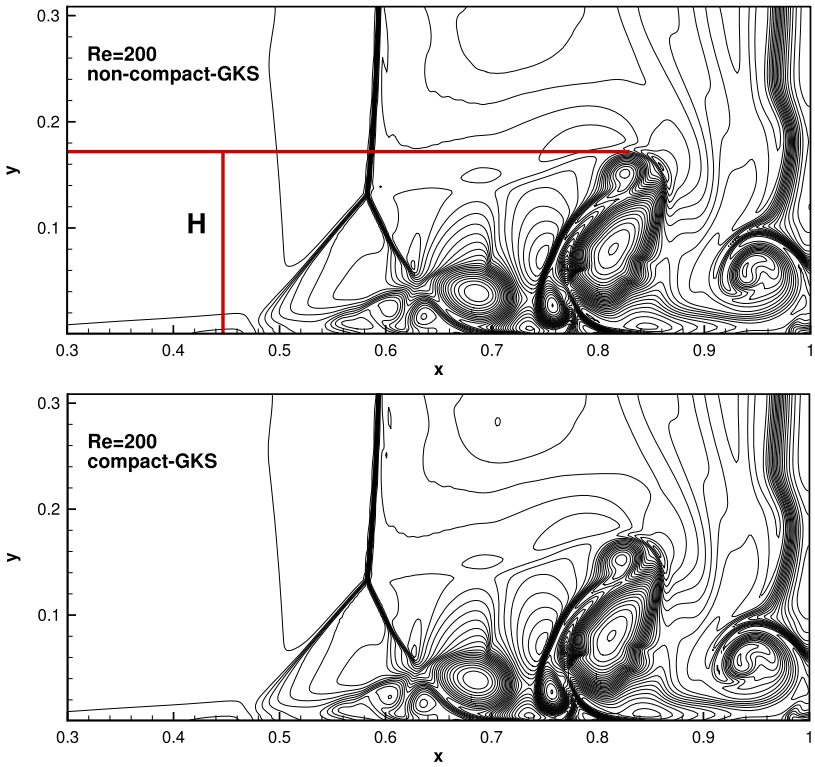

Fig. 10. Viscous shock tube problem: density contours with 500×250 uniform mesh points at $t = 1$ for $Re = 200$ case.

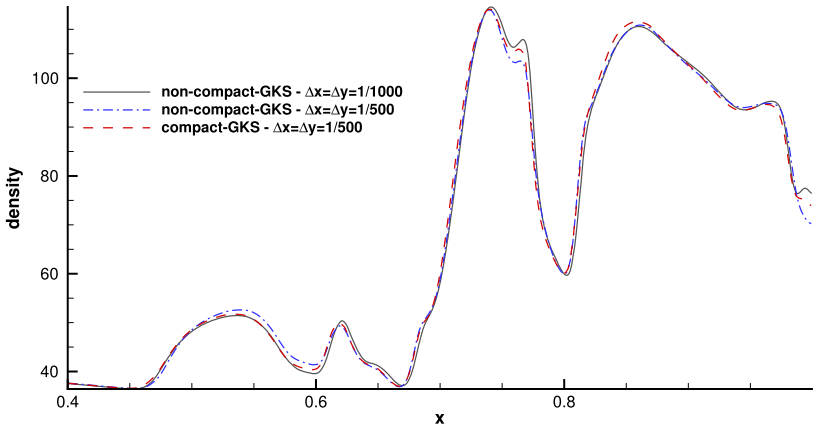

Fig. 11. Viscous shock tube problem: density profiles along the lower wall at $t = 1$ for $Re = 200$ case.

Table 3
Viscous shock tube problem: comparison of the primary vortex heights among different schemes with 500×250 uniform mesh points for $Re = 200$ case.

Scheme	AUSMPW + [22]	M-AUSMPW + [22]	WENO-GKS	HWENO-GKS
Height	0.163	0.168	0.171	0.173

is to compensate the physical weakness in the 1st-order Riemann solver by the numerical techniques in the current study for higher-order schemes, and some numerical compensation, such as the evolution equations for the equivalent slopes in DG, may not be as reliable as others, such as the reconstruction of slopes from large stencils in the WENO. With the implementation of high-order gas evolution model, such as GRP and GKS, both numerical and physical domains of dependence are getting close in the corresponding higher-order compact schemes. The unified gas kinetic scheme (UGKS) makes these two domains of dependence even closer than that of GKS [53,57]. For example, the UGKS can use a much larger CFL num-

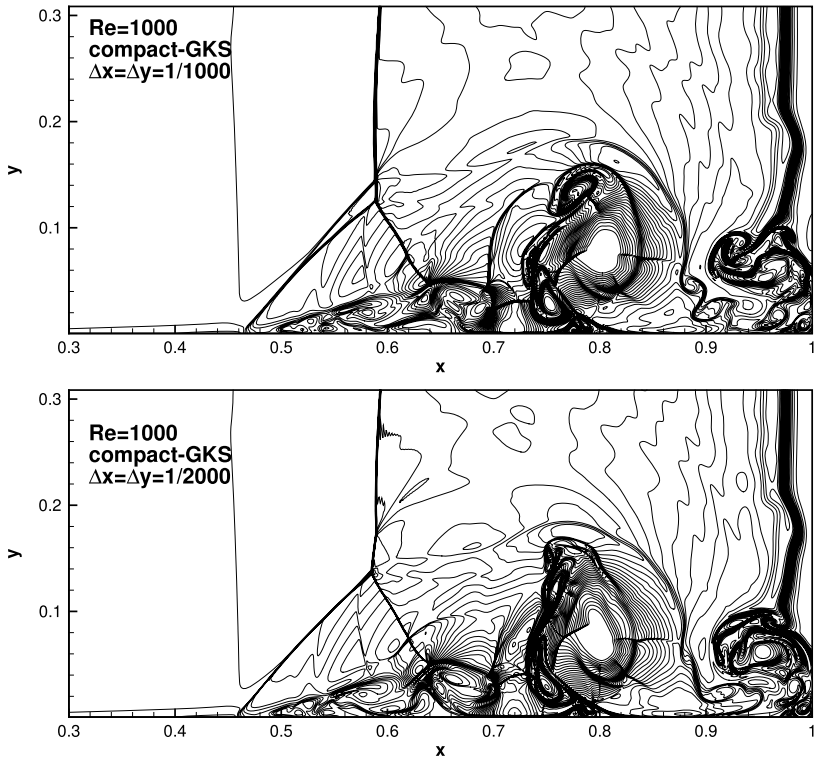

Fig. 12. Viscous shock tube problem: density contours with 1000×500 and 2000×1000 uniform mesh points at $t = 1$ for $Re = 1000$.

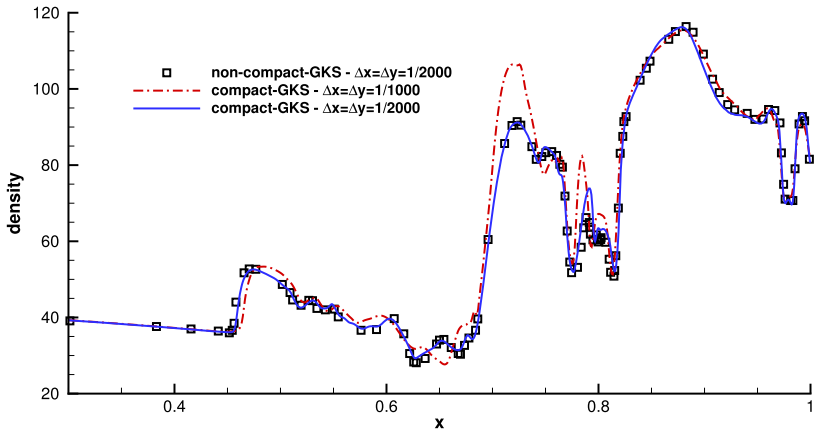

Fig. 13. Viscous shock tube problem: density profiles along the lower surface at $t = 1$ for $Re = 1000$ case.

ber than that of GKS in the low Reynolds number viscous flow computations. This is due to the further physical soundness in the modeling of UGKS, such as removing the assumption of Chapman–Enskog expansion in the initial gas distribution function in GKS, and following the multiscale nature of gas dynamics.

Acknowledgements

The authors would like to thank Prof. J.Q. Li and J.X. Qiu for helpful discussion and reviewers for their constructive comments. The current research was supported by Hong Kong research grant council (16206617, 16207715), National Science Foundation of China (91530319, 11772281, 11701038), and China Postdoctoral Science Foundation (2016M600065).

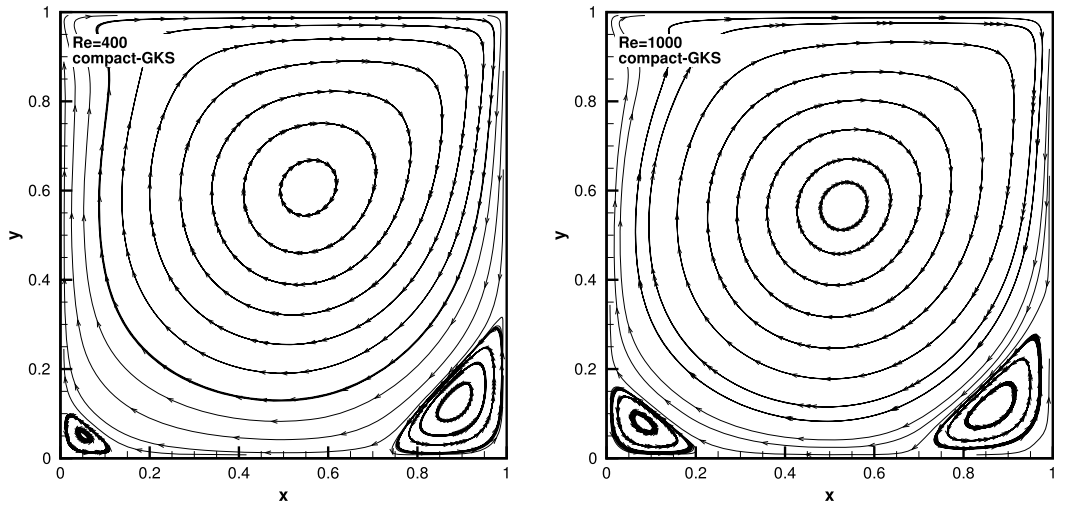

Fig. 14. Lid-driven cavity flow: streamlines with 65×65 uniform mesh points for $Re = 400$ and $Re = 1000$ by compact HWENO-GKS.

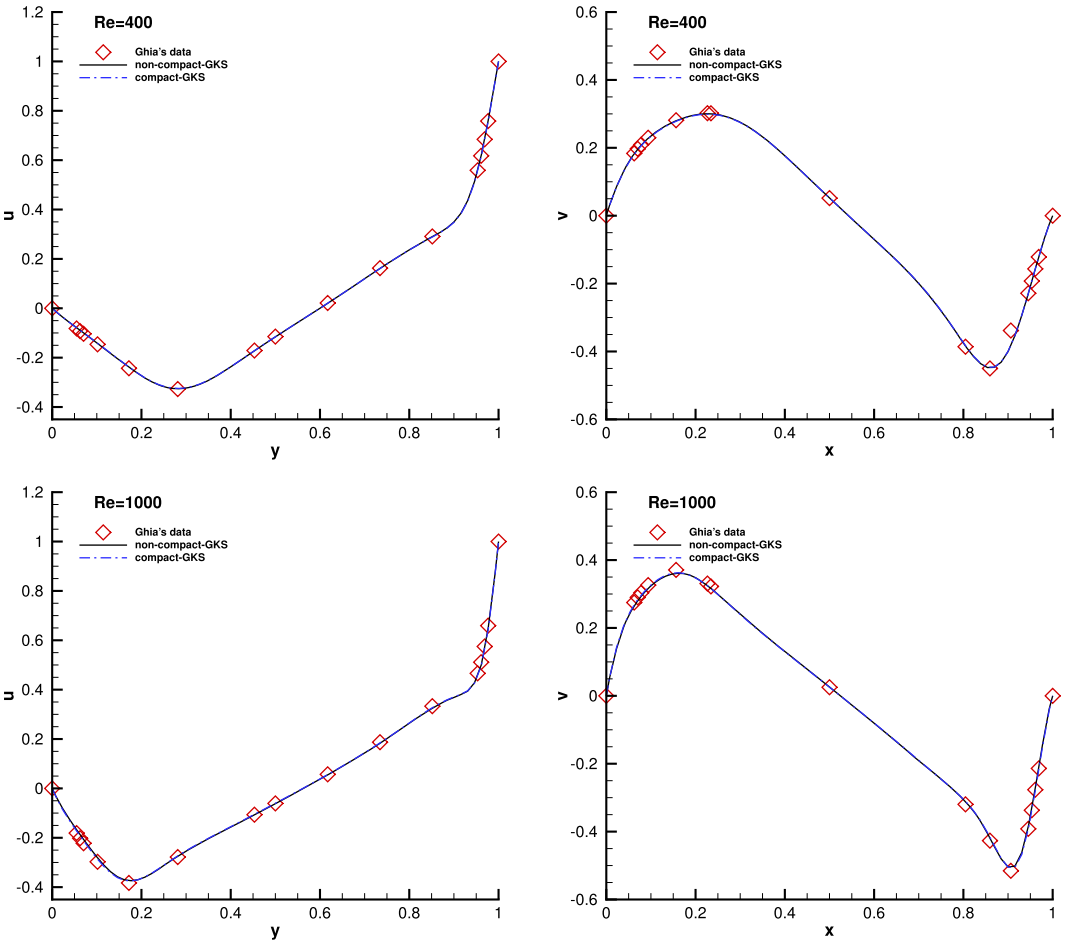

Fig. 15. Lid-driven cavity flow: Comparisons between non-compact WENO-GKS and compact HWENO-GKS by U-velocity along vertical centerline line and V-velocity along horizontal center-line with 65×65 uniform mesh points, at $Re = 400$ and 1000.

Appendix A. HWENO reconstruction at Gaussian points

For the interface values reconstruction, starting from the same stencils as that in [41], the pointwise values for three sub-stencils at Gaussian point $x_{i+1/2\sqrt{3}}$ are

$$p_0(x_{i+1/2\sqrt{3}}) = -\frac{1}{\sqrt{3}}W_{i-1} + \frac{3+\sqrt{3}}{\sqrt{3}}W_i - \frac{\Delta x}{2\sqrt{3}}(W_x)_{i-1},$$
$$p_1(x_{i+1/2\sqrt{3}}) = \frac{3-\sqrt{3}}{\sqrt{3}}W_i + \frac{1}{\sqrt{3}}W_{i+1} - \frac{\Delta x}{2\sqrt{3}}(W_x)_{i+1},$$
$$p_2(x_{i+1/2\sqrt{3}}) = -\frac{1}{4\sqrt{3}}W_{i-1} + W_i + \frac{1}{4\sqrt{3}}W_{i+1}.$$

The pointwise value for the large stencil at the Gaussian point $x_{i+1/2\sqrt{3}}$ is

$$q(x_{i+1/2\sqrt{3}}) = \frac{1}{720}[(2-95\sqrt{3})W_{i-1} + (2+95\sqrt{3})W_{i+1} + 716W_i$$
$$+\Delta x(1-35\sqrt{3})(W_x)_{i-1} - \Delta x(1+35\sqrt{3})(W_x)_{i+1})].$$

In order to satisfy the following equations

$$q(x_{i+1/2\sqrt{3}}) = \sum_{k=0}^{2}\hat{\gamma}_k p_k(x_{i+1/2\sqrt{3}}),$$

the linear weights become $\hat{\gamma}_0 = \frac{105-\sqrt{3}}{360}$, $\hat{\gamma}_1 = \frac{105+\sqrt{3}}{360}$, $\hat{\gamma}_2 = \frac{5}{12}$. The smoothness indicators and non-linear weights take the identical forms as that in [41]. The pointwise values and linear weights at another Gaussian point $x_{i-1/2\sqrt{3}}$ can be obtained similarly using symmetrical property.

Appendix B. Reconstruction for slope at Gaussian points

The slope at Gaussian points is reconstructed as follows. Denote that $P_{i-1/2,j_l}, l = 0, 1$ as the Gaussian quadrature points of the interface $(i-1/2, j)$. For simplicity, the suffix $i-1/2$ is omitted next without confusion. Two sub-stencils are defined as

$$S_0 = \{P_{(j-1)_2}, P_{j_1}, P_{j_2}\}, \quad S_1 = \{P_{j_1}, P_{j_2}, P_{(j+1)_1}\},$$

where $j_1 = j - 1/2\sqrt{3}$, $j_2 = j + 1/2\sqrt{3}$. A quadratic polynomial $p_k(y)$ can be constructed corresponding to $S_k, k = 0, 1$. For the large stencil

$$\mathbb{T} = \{S_0, S_1\},$$

a cubic polynomial $q(y)$ can be constructed as well. The first-order derivative of $q(y)$ can be written as a linear combination of all first-order derivatives of $p_k(y)$ corresponding to stencils S_k at Gaussian point $y_{j+1/2\sqrt{3}}$

$$\frac{\partial q}{\partial y}(y_{j+1/2\sqrt{3}}) = \sum_{k=0}^{1}\check{\gamma}_k\Big(\frac{\partial p}{\partial y}\Big)_k(y_{j+1/2\sqrt{3}}),$$

with the linear weights $\check{\gamma}_0 = \frac{5-\sqrt{3}}{11}$, $\check{\gamma}_1 = \frac{6+\sqrt{3}}{11}$, and

$$\Big(\frac{\partial p}{\partial y}\Big)_0(y_{j+1/2\sqrt{3}}) = \frac{1}{(\sqrt{3}-1)\Delta y}(W_{(j-1)_2} - 3W_{j_1} + 2W_{j_2}),$$
$$\Big(\frac{\partial p}{\partial y}\Big)_1(y_{j+1/2\sqrt{3}}) = \frac{1}{(\sqrt{3}-1)\Delta y}[(-2+\sqrt{3})W_{j_1} + (3-2\sqrt{3})W_{j_2} + W_{(j+1)_1}],$$

where W_{j_l} are the pointwise values at the Gaussian quadrature points P_{j_l}. The smoothness indicators for $\check{\beta}_k,\ k = 0, 1$ are defined by

$$\check{\beta}_k = \Delta x^3 \int_{y_{j-1/2}}^{y_{j+1/2}} \Big(\frac{\mathrm{d}^2}{\mathrm{d}y^2}p_k(x)\Big)^2 \mathrm{d}x,$$

and the detailed formulae are given as follows

$$\breve{\beta}_0 = \frac{4}{(\sqrt{3}-1)^2}[\sqrt{3}W_{(j-1)_2} - 3W_{j_1} + (3-\sqrt{3})W_{j_2}]^2,$$
$$\breve{\beta}_1 = \frac{4}{(\sqrt{3}-1)^2}[(3-\sqrt{3})W_{j_1} - 3W_{j_2} + \sqrt{3}W_{(j+1)_1}]^2.$$

Finally, the non-normalized nonlinear weights $\overline{\breve{\omega}}_k, k = 0, 1$ are

$$\overline{\breve{\omega}}_k = \frac{\breve{\gamma}_k}{(\breve{\beta}_k + \epsilon)^2}.$$

The pointwise values and linear weights at Gaussian point $y_{j-1/2\sqrt{3}}$ can be obtained similarly using the symmetrical property again.

Appendix C. Calculation of GKS flux function

This appendix presents some details for the implementation of gas-kinetic flux solver. The references [53,54] are recommended as a start point for GKS programming as well.

The final form of the simplified 3rd-order gas kinetic distribution function along a cell interface $x_{i+1/2}$ in Eq. (14) is listed here again for a clearer illustration, which reads

$$\begin{aligned} f(x_{i+1/2}, y_{j_\ell}, t, u, v, \xi) = {} & g_0 + \bar{A}g_0 t + \frac{1}{2}\bar{a}_{tt}g_0 t^2 \\ & - \tau[(\bar{a}_1 u + \bar{a}_2 v + \overline{A})g_0 + (\bar{a}_{xt}u + \bar{a}_{yt}v + \bar{a}_{tt})g_0 t] \\ & - e^{-t/\tau}g_0[1 - (\bar{a}_1 u + \bar{a}_2 v)t] \\ & + e^{-t/\tau}g_l[1 - (a_{1l}u + a_{2l}v))t]H(u) \\ & + e^{-t/\tau}g_r[1 - (a_{1r}u + a_{2r}v))t](1 - H(u)). \end{aligned} \tag{30}$$

The $f(x_{i+1/2,j_\ell}, y, t, u, v, \xi)$ on LHS is a function in physical space (x, y, t) and phase space (u, v, ξ). The local original point of the physical space is chosen as each Gaussian point at corresponding cell interfaces $(x_{i+1/2,j_\ell}, y_{i+1/2,j_\ell}) = (0, 0)$. And all the coefficients on the RHS are also based on this local coordinates, i.e., $g_0 = g_0(x_{i+1/2,j_\ell} = 0, y_{i+1/2,j_\ell} = 0, t = 0, u, v, \xi)$. The interface value could be obtained by Eq. (22) and the corresponding flux by Eq. (5).

Moment calculation

According to the RHS of Eq. (30), we need to evaluate the complex combination of different moments of the Maxwellian distribution functions g_0, g_l and g_r. The general formulas of moment evaluations are given first.

For a two-dimensional Maxwellian distribution

$$g = \rho(\frac{\lambda}{\pi})^{\frac{K+2}{2}} e^{-\lambda((u-U)^2+(v-V)^2+\xi^2)},$$

the moments of g is defined as

$$\rho\langle|...|\rangle = \int (...)g\mathrm{d}\Xi,$$

the general moment formula becomes

$$\langle|u^n v^m \xi^{2l}|\rangle = \langle|u^n|\rangle\langle|v^m|\rangle\langle|\xi^{2l}|\rangle,$$

where n, m, l are integers (owing to the symmetrical property of ξ, the moments of ξ are always even-order). With the integral from $-\infty$ to $+\infty$, we have

$$\begin{aligned} \langle|u^0|\rangle &= 1, \\ \langle|u^1|\rangle &= U, \\ &\cdots \\ \langle|u^{n+2}|\rangle &= U\langle|u^{n+1}|\rangle + \frac{n+1}{2\lambda}|\langle u^n|\rangle. \end{aligned}$$

Integrating terms with Heaviside function, the integral from 0 to $+\infty$ is denoted as $\langle|...|\rangle_{>0}$, and from $-\infty$ to 0 as $\langle|...|\rangle_{<0}$,

$$\langle|u^0|\rangle_{>0} = \frac{1}{2}\mathrm{erfc}(-\sqrt{\lambda}U),$$
$$\langle|u^1|\rangle_{>0} = U\langle|u^0|\rangle_{>0} + \frac{1}{2}\frac{e^{-\lambda U^2}}{\sqrt{\pi\lambda}},$$
$$\cdots$$
$$\langle|u^{n+2}|\rangle_{>0} = U\langle|u^{n+1}|\rangle_{>0} + \frac{n+1}{2\lambda}\langle|u^n|\rangle_{>0}$$

and

$$\langle|u^0|\rangle_{<0} = \frac{1}{2}\mathrm{erfc}(\sqrt{\lambda}U),$$
$$\langle|u^1|\rangle_{<0} = U\langle|u^0|\rangle_{<0} - \frac{1}{2}\frac{e^{-\lambda U^2}}{\sqrt{\pi\lambda}},$$
$$\cdots$$
$$\langle|u^{n+2}|\rangle_{<0} = U\langle|u^{n+1}|\rangle_{<0} + \frac{n+1}{2\lambda}\langle|u^n|\rangle_{<0},$$

where erfc is the standard complementary error function. The moments of $\langle|\xi^{2l}|\rangle$ from $-\infty$ to $+\infty$ are

$$\langle|\xi^0|\rangle = 1,$$
$$\langle|\xi^2|\rangle = (\frac{K}{2\lambda}),$$
$$\langle|\xi^{2l}|\rangle = \frac{K+2(l-1)}{2\lambda}\langle|\xi^{2(l-1)}|\rangle.$$

Derivatives in macroscopic flow variables and microscopic distribution function

Once the reconstruction for macroscopic flow derivatives is finished, the microscopic derivatives $\bar{a}_1 \ldots \bar{a}_{tt}, a_{1l} \ldots a_{2r}$ in Eq. (14) can be obtained in the following way.

From the Taylor expansion of a Maxwellian distribution, all microscopic derivatives shall have in the following form

$$a_1 = a_{11} + a_{12}u + a_{13}v + a_{14}\frac{1}{2}(u^2+v^2+\xi^2) = a_{1\beta}\psi_\beta,$$
$$a_2 = a_{21} + a_{22}u + a_{23}v + a_{24}\frac{1}{2}(u^2+v^2+\xi^2) = a_{2\beta}\psi_\beta,$$
$$\cdots$$
$$a_{tt} = a_{tt1} + a_{tt2}u + a_{tt3}v + a_{tt4}\frac{1}{2}(u^2+v^2+\xi^2) = a_{tt\beta}\psi_\beta.$$

According to the relation between distribution function and the macroscopic variables in Eq. (3), we have

$$\int \psi a_1 g d\Xi = \frac{\partial W}{\partial x},$$

which could be expanded as

$$\frac{1}{\rho}\frac{\partial W}{\partial x} = \frac{1}{\rho}\begin{pmatrix} \frac{\partial \rho}{\partial x} \\ \frac{\partial(\rho U)}{\partial x} \\ \frac{\partial(\rho V)}{\partial x} \\ \frac{\partial(\rho E)}{\partial x} \end{pmatrix} = \langle|\alpha_{1\beta}\psi_\beta\psi_\alpha|\rangle = \langle|\psi_\alpha\psi_\beta|\rangle \begin{pmatrix} a_{11} \\ a_{12} \\ a_{13} \\ a_{14} \end{pmatrix}. \tag{31}$$

Denoting $\mathbf{M} = \langle|\psi_\alpha\psi_\beta|\rangle$, the above equations become a linear system

$$\mathbf{Ma} = \mathbf{b}, \tag{32}$$

and the coefficient matrix $\mathbf{M}$ is given by

$$\mathbf{M}=\begin{pmatrix} \langle|u^0|\rangle & \langle|u^1|\rangle & \langle|v^1|\rangle & \langle|\psi_4|\rangle \\ \langle|u^1|\rangle & \langle|u^2|\rangle & \langle|u^1v^1|\rangle & \langle|u^1\psi_4|\rangle \\ \langle|v^1|\rangle & \langle|u^1v^1|\rangle & \langle|v^2|\rangle & \langle|v^1\psi_4|\rangle \\ \langle|\psi_4|\rangle & \langle|u^1\psi_4|\rangle & \langle|v^1\psi_4|\rangle & \langle|\psi_4^2|\rangle \end{pmatrix}=\begin{pmatrix} 1 & U & V & B_1 \\ U & U^2+1/2\lambda & UV & B_2 \\ V & UV & V^2+1/2\lambda & B_3 \\ B_1 & B_2 & B_3 & B_4 \end{pmatrix},$$

where

$$\begin{aligned} B_1&=\frac{1}{2}(U^2+V^2+\frac{K+2}{2\lambda}),\\ B_2&=\frac{1}{2}(U^3+V^2U+\frac{(K+4)U}{2\lambda}),\\ B_3&=\frac{1}{2}(V^3+U^2V+\frac{(K+4)V}{2\lambda}),\\ B_4&=\frac{1}{4}((U^2+V^2)^2+\frac{(K+4)(U^2+V^2)}{\lambda})+\frac{K^2+6K+8}{4\lambda^2}). \end{aligned}$$

Denoting

$$R_4=2b_4-(U^2+V^2+\frac{K+2}{2\lambda})b_1,\quad R_3=b_3-Vb_1,\quad R_2=b_2-Ub_1,$$

the solution of Eq. (32) can be written as

$$\begin{aligned} a_4&=\frac{4\lambda^2}{K+2}(R4-2UR_2-2VR_3),\\ a_3&=2\lambda R_3-Va_4,\\ a_2&=2\lambda R_2-Ua_4,\\ a_1&=b_1-Ua_2-Va_3-\frac{1}{2}a_4(U^2+V^2+\frac{K+2}{2\lambda}). \end{aligned}$$

Thus, once the reconstructions for macroscopic flow variables and their derivatives are provided, the micro first-order spatial derivatives can be calculated. We use the abbreviation $\langle a_1\rangle=\dfrac{\partial W}{\partial x}$ to represent the relation in Eq. (31). Similarly we have $\langle a_2\rangle=\dfrac{\partial W}{\partial y}$.

According to the compatibility condition Eq. (2), we have the following equation for the micro first-order temporal derivatives

$$\langle a_1u+a_2v+A\rangle=0.$$

The coefficient A can be obtained by solving the following equation

$$\langle A\rangle=-\langle a_1u+a_2v\rangle.$$

With the similar procedure, the coefficients in third-order simplified flux solver Eq. (14) can be fully determined by the constraints Eq. (15). More details could be found in [32,60].

Time integration for third-order flux solver

Since the distribution function is time dependent, the total flux in one time step from t_n to $t_n+\Delta t$ yields

$$\begin{aligned} \mathbb{F}_{i+1/2,j_\ell}(W^n,\delta)&=\int_{t_n}^{t_n+\delta}F_{i+1/2,j_\ell}(W^n,t)\mathrm{d}t\\ &=\iint_{t_n}^{t_n+\delta}u\psi f(x_{i+1/2},y_{j_\ell},t,u,v,\xi)\mathrm{d}\Xi\mathrm{d}t\\ &=\iint_{t_n}^{t_n+\delta}u\psi f(x_{i+1/2},y_{j_\ell},t,u,v,\xi)\mathrm{d}t\mathrm{d}\Xi, \end{aligned}$$

where

$$\int_{t_n}^{t_n+\delta} u\psi f(x_{i+1/2}, y_{j_\ell}, t, u, v, \xi)\mathrm{d}t = g_0\delta + \frac{1}{2}\bar{A}g_0\delta^2 + \frac{1}{6}\bar{a}_{tt}g_0\delta^3$$
$$- \tau[(\bar{A} + u\bar{a}_1 + v\bar{a}_2)g_0\delta + \frac{1}{2}(\bar{a}_{tt} + u\bar{a}_{xt} + v\bar{a}_{yt})g_0\delta^2]$$
$$+ \tau e^{-\delta/\tau} g_0[1 - (u\bar{a}_1 + v\bar{a}_2)(\delta + \tau)]$$
$$- \tau e^{-\delta/\tau} g_l[1 - (ua_{1l} + va_{2l})(\delta + \tau)]H(u)$$
$$- \tau e^{-\delta/\tau} g_r[1 - (ua_{1r} + va_{2r})(\delta + \tau)](1 - H(u)).$$

References

[1] D.S. Balsara, S. Garain, C.W. Shu, An efficient class of WENO schemes with adaptive order, J. Comput. Phys. 326 (2016) 780–804.
[2] M. Ben-Artzi, J. Falcovitz, A second-order Godunov-type scheme for compressible fluid dynamics, J. Comput. Phys. 55 (1984) 1–32.
[3] M. Ben-Artzi, J. Li, G. Warnecke, A direct Eulerian GRP scheme for compressible fluid flows, J. Comput. Phys. 218 (2006) 19–43.
[4] M. Ben-Artzi, J. Li, Hyperbolic conservation laws: Riemann invariants and the generalized Riemann problem, Numer. Math. 106 (2007) 369–425.
[5] P.L. Bhatnagar, E.P. Gross, M. Krook, A model for collision processes in gases I: small amplitude processes in charged and neutral one-component systems, Phys. Rev. 94 (1954) 511–525.
[6] R. Borges, M. Carmona, B. Costa, W.S. Don, An improved weighted essentially non-oscillatory scheme for hyperbolic conservation laws, J. Comput. Phys. 227 (2008) 3191–3211.
[7] S. Chapman, T.G. Cowling, The Mathematical Theory of Non-Uniform Gases, third edition, Cambridge University Press, 1990.
[8] A.J. Christlieb, S. Gottlieb, Z. Grant, D.C. Seal, Explicit strong stability preserving multistage two-derivative time-stepping scheme, J. Sci. Comput. 68 (2016) 914–942.
[9] B. Cockburn, C.W. Shu, TVB Runge–Kutta local projection discontinuous Galerkin finite element method for conservation laws II: general framework, Math. Comput. 52 (1989) 411–435.
[10] B. Cockburn, C.W. Shu, The Runge–Kutta discontinuous Galerkin method for conservation laws V: multidimensional systems, J. Comput. Phys. 141 (1998) 199–224.
[11] M. Dumbser, M. Käser, Arbitrary high order non-oscillatory finite volume schemes on unstructured meshes for linear hyperbolic systems, J. Comput. Phys. 221 (2) (2007) 693–723.
[12] M. Dumbser, D.S. Balsara, E.F. Toro, C.D. Munz, A unified framework for the construction of one-step finite volume and discontinuous Galerkin schemes on unstructured meshes, J. Comput. Phys. 227 (18) (2008) 8209–8253.
[13] V. Daru, C. Tenaud, Numerical simulation of the viscous shock tube problem by using a high resolution monotonicity-preserving scheme, Comput. Fluids 38 (2009) 664–676.
[14] Z. Du, J. Li, A Hermite WENO reconstruction for fourth-order temporal accurate schemes based on the GRP solver for hyperbolic conservation laws, J. Comput. Phys. 355 (2018) 385–396.
[15] U. Ghia, K.N. Ghia, C.T. Shin, High-Re solutions for incompressible flow using the Navier–Stokes equations and a multigrid method, J. Comput. Phys. 48 (1982) 387–411.
[16] S. Gottlieb, C.W. Shu, Total variation diminishing Runge–Tutta schemes, Math. Comput. 67 (1998) 73–85.
[17] E. Hairer, G. Wanner, Multistep multistage multiderivative methods for ordinary differential equations, Computing 11 (1973) 287–303.
[18] A. Harten, High resolution schemes for hyperbolic conservation laws, J. Comput. Phys. 49 (1983) 357–393.
[19] A. Harten, B. Engquist, S. Osher, S.R. Chakravarthy, Uniformly high order accurate essentially non-oscillatory schemes, III, J. Comput. Phys. 71 (1987) 231–303.
[20] X. Ji, F.X. Zhao, W. Shyy, K. Xu, A family of high-order gas-kinetic schemes and its comparison with Riemann solver based high-order methods, J. Comput. Phys. 356 (2018) 150–173.
[21] G.S. Jiang, C.W. Shu, Efficient implementation of weighted ENO schemes, J. Comput. Phys. 126 (1996) 202–228.
[22] K.H. Kim, C. Kim, Accurate, efficient and monotonic numerical methods for multi-dimensional compressible flows, Part I: spatial discretization, J. Comput. Phys. 208 (2005) 527–569.
[23] G. Zhou, K. Xu, F. Liu, Grid-converged solution and analysis of the unsteady viscous flow in a two-dimensional shock tube, Phys. Fluids 30 (2018) 016102.
[24] C.B. Lee, S. Wang, Study of the shock motion in a hypersonic shock system/turbulent boundary layer interaction, Exp. Fluids 19 (1995) 143–149.
[25] C.B. Lee, J.Z. Wu, Transition in wall-bounded flows, Appl. Mech. Rev. 61 (3) (2008) 030802.
[26] J. Li, Z. Du, A two-stage fourth order time-accurate discretization for Lax–Wendroff type flow solvers I. hyperbolic conservation laws, SIAM J. Sci. Comput. 38 (2016) 3046–3069.
[27] J. Li, C.W. Zhong, Y. Wang, C.S. Zhuo, Implementation of dual time-stepping strategy of the gas-kinetic scheme for unsteady flow simulations, Phys. Rev. E 95 (2017) 053307.
[28] J. Li, Q.B. Li, K. Xu, Comparison of the generalized Riemann solver and the gas-kinetic scheme for inviscid compressible flow simulations, J. Comput. Phys. 230 (2011) 5080–5099.
[29] Q. Li, K. Xu, S. Fu, A high-order gas-kinetic Navier–Stokes flow solver, J. Comput. Phys. 229 (2010) 6715–6731.
[30] N. Liu, H.Z. Tang, A high-order accurate gas-kinetic scheme for one- and two-dimensional flow simulation, Commun. Comput. Phys. 15 (2014) 911–943.
[31] X.D. Liu, S. Osher, T. Chan, Weighted essentially non-oscillatory schemes, J. Comput. Phys. 115 (1994) 200–212.
[32] J. Luo, K. Xu, A high-order multidimensional gas-kinetic scheme for hydrodynamic equations, Sci. China, Technol. Sci. 56 (2013) 2370–2384.
[33] P.D. Lax, X.D. Liu, Solution of two-dimensional Riemann problems of gas dynamics by positive schemes, SIAM J. Sci. Comput. 19 (1998) 319–340.
[34] P.D. Lax, B. Wendroff, Systems of conservation laws, Commun. Pure Appl. Math. 13 (1960) 217–237.
[35] T. Ohwada, K. Xu, The kinetic scheme for the full-Burnett equations, J. Comput. Phys. 201 (2004) 315–332.
[36] L. Pan, J.Q. Li, K. Xu, A few benchmark test cases for higher-order Euler solvers, Numer. Math. Theor. Meth. Appl. 10 (2017) 711–736.
[37] L. Pan, K. Xu, A compact third-order gas-kinetic scheme for compressible Euler and Navier–Stokes equations, Commun. Comput. Phys. 18 (2015) 985–1011.
[38] L. Pan, K. Xu, A third-order compact gas-kinetic scheme on unstructured meshes for compressible Navier–Stokes solutions, J. Comput. Phys. 318 (2016) 327–348.

[39] L. Pan, K. Xu, Q. Li, J. Li, An efficient and accurate two-stage fourth-order gas-kinetic scheme for the Navier–Stokes equations, J. Comput. Phys. 326 (2016) 197–221.
[40] L. Pan, J.X. Cheng, S.H. Wang, K. Xu, A two-stage fourth-order gas-kinetic scheme for compressible multicomponent flows, Commun. Comput. Phys. 22 (2017) 1123–1149.
[41] J.X. Qiu, C.-W. Shu, Hermite WENO schemes and their application as limiters for Runge–Kutta discontinuous Galerkin method: one-dimensional case, J. Comput. Phys. 193 (2004) 115–135.
[42] J.X. Qiu, C.-W. Shu, Hermite WENO schemes and their application as limiters for Runge–Kutta discontinuous Galerkin method II: two dimensional case, Comput. Fluids 34 (2005) 642–663.
[43] J.X. Qiu, C.-W. Shu, Hermite WENO schemes and their application as limiters for Runge–Kutta discontinuous Galerkin method, III: unstructured meshes, J. Sci. Comput. 39 (2009) 293–321.
[44] X.D. Ren, K. Xu, W. Shyy, C.W. Gu, Multi-dimensional high-order discontinuous Galerkin method based on gas kinetic theory for viscous flow computations, J. Comput. Phys. 292 (2015) 176–193.
[45] D.C. Seal, Y. Güclü, A.J. Christlieb, High-order multiderivative time integrators for hyperbolic conservation laws, J. Sci. Comput. 60 (2014) 101–140.
[46] C.W. Shu, S. Osher, Efficient implementation of essentially non-oscillatory shock capturing schemes, J. Comput. Phys. 77 (1988) 439–471.
[47] C.W. Shu, S. Osher, Efficient implementation of essentially non-oscillatory shock capturing schemes II, J. Comput. Phys. 83 (1989) 32–78.
[48] V.A. Titarev, E.F. Toro, Finite volume WENO schemes for three-dimensional conservation laws, J. Comput. Phys. 201 (2014) 238–260.
[49] E. Toro, Riemann Solvers and Numerical Methods for Fluid Dynamics, third edition, Springer, 2009.
[50] B. van Leer, Towards the ultimate conservative difference scheme V. A second order sequel to Godunov's method, J. Comput. Phys. 32 (1979) 101–136.
[51] P. Woodward, P. Colella, Numerical simulations of two-dimensional fluid flow with strong shocks, J. Comput. Phys. 54 (1984) 115–173.
[52] K. Xu, A slope-update scheme for compressible flow simulation, J. Comput. Phys. 178 (2002) 252–259.
[53] K. Xu, Direct Modeling for Computational Fluid Dynamics: Construction and Application of Unified Gas Kinetic Schemes, World Scientific, 2015.
[54] K. Xu, A gas-kinetic BGK scheme for the Navier–Stokes equations and its connection with artificial dissipation and Godunov method, J. Comput. Phys. 171 (2001) 289–335.
[55] K. Xu, Z.H. Li, Microchannel flow in the slip regime: gas-kinetic BGK-Burnett solutions, J. Fluid Mech. 513 (2004) 87–110.
[56] K. Xu, J.C. Huang, A unified gas-kinetic scheme for continuum and rarefied flows, J. Comput. Phys. 229 (2010) 7747–7764.
[57] K. Xu, C. Liu, A paradigm for modeling and computation of gas dynamics, Phys. Fluids 29 (2017) 026101.
[58] J.Y. Yang, T.Y. Hsieh, Y.H. Shi, K. Xu, High-order kinetic flux vector splitting schemes in general coordinates for ideal quantum gas dynamics, J. Comput. Phys. 227 (2007) 967–982.
[59] R. Zhang, M.P. Zhang, C.W. Shu, On the order of accuracy and numerical performance of two classes of finite volume WENO schemes, Commun. Comput. Phys. 9 (2011) 807–827.
[60] G. Zhou, K. Xu, F. Liu, Simplification of the flux function for a high-order gas-kinetic evolution model, J. Comput. Phys. 339 (2017) 146–162.